

POLITECNICO DI MILANO
Facoltà di Ingegneria dei Sistemi
Corso di Laurea Magistrale in Ingegneria Matematica



Computational Models for Power Electronics Cooling Systems

Relatore: Prof. Riccardo Sacco

Correlatori: Ing. Carlo de Falco
Ing. Francesco Agostini
Prof. Maurizio Verri

Tesi di Laurea di:
Lucia Carichino matr. 724805

Anno Accademico 2009-2010

Contents

Contents	i
List of Figures	v
I Introduction	1
1 Description of an electronic cooling system and technological motivations	3
1.1 Cooling systems overview	3
1.2 A thermosyphon cooler	6
1.3 Technological motivations	8
II Mathematical Models	9
2 Description of the air subsystem	11
2.1 Air physical model	11
2.2 Air correlations	14
2.2.1 Air heat transfer coefficient correlation	15
2.2.2 Pressure drop	18
3 Description of the panel subsystem	21
3.1 Panel physical model	21
4 Description of the channel subsystem	25
4.1 Single-phase incompressible fluid	25
4.1.1 Horizontal channel	25
4.1.2 Vertical channel	29
4.2 Two-phase compressible fluid	31

4.2.1	Two-phase liquid-vapor flow	32
4.3	Two-phase flow correlations	33
4.3.1	Two-phase heat transfer coefficient correlation	33
4.3.2	Pressure drop	34
III Numerical Methods		37
5	Mixed finite volume discretization of 2D diffusion, advection and reaction models	39
5.1	The model problem	39
5.2	Finite volume discretization	40
5.3	Mixed finite volume discretization	43
5.4	Comparison between upwind and SG methods	48
5.5	Validation of the discretization scheme	50
6	Galerkin and Petrov-Galerkin discretization of 1D fluid equation	55
6.1	Single-phase incompressible fluid	55
6.2	Two-phase compressible fluid	60
7	Computational algorithms	63
7.1	Algebraic systems	63
7.1.1	Air	63
7.1.2	Panel	65
7.1.3	Channel	66
7.2	Boundary conditions	68
7.3	Iteration between domains	69
IV Simulation Results		71
8	Results	73
8.1	Test for air and panel subsystems	73
8.2	Test for channel subsystem	78
8.2.1	Single-phase incompressible fluid	78
8.2.2	Two-phase compressible fluid	86

V Conclusions and Perspectives	91
9 Conclusions and future work	93
Bibliography	95

List of Figures

1.1	Examples of water and air-cooled electronic devices.	4
1.2	Example of an heat sink system.	5
1.3	Thermosyphon	5
1.4	Comparison of the heat transfer coefficient values varying the cooling system.	6
1.5	Geometry of the condenser.	6
1.6	Examples of condenser panels.	7
1.7	Two-phase flow patterns.	8
2.1	Air domain.	12
2.2	Geometry of the air problem.	15
2.3	Two entrance region configurations.	18
3.1	Panel domain.	22
3.2	Thickness of the panel.	22
3.3	An example of partition of surface Λ	23
4.1	Horizontal channel domain.	26
4.2	Vertical channel domain.	30
4.3	Modified Shah correlation.	35
5.1	Computational stencil.	41
5.2	Trend of the inverse Bernoulli function.	42
5.3	Two neighboring elements.	45
5.4	Test of convergence order for upwind and SG methods.	51
5.5	Test cases numerical solutions using the SG method.	53
6.1	Piecewise-linear base function.	57
6.2	Upwind Petrov-Galerkin linear basis functions.	60

7.1	Iteration algorithm between domains.	69
8.1	Air and panel coupled test case: geometry.	74
8.2	Air and panel coupled test case: channel and air-panel meshes.	75
8.3	Air and panel coupled test case: air temperature and panel wall temperature solution.	76
8.4	Air and panel coupled test case: contour plot of air temperature and panel wall temperature solution.	77
8.5	Air and panel coupled test case: heat transfer coefficient h_{aw}	79
8.6	Air and panel coupled test case: total air pressure drop.	80
8.7	Incompressible single-phase test case: mass flow and total pressure drop.	81
8.8	Incompressible single-phase test case: three contributions to the total pressure drop.	82
8.9	Incompressible single-phase test case: temperature distribution.	84
8.10	Incompressible single-phase test case: outlet fluid temperature	85
8.11	Compressible two-phase test case: geometry.	85
8.12	Compressible two-phase test case: R134a two-phase properties.	86
8.13	Compressible two-phase test case: R134a saturation curve.	87
8.14	Compressible two-phase test case: R134a temperature and pressure.	88
8.15	Compressible two-phase test case: R134a velocity, vapor quality and two-phase enthalpy.	89
8.16	Compressible two-phase test case: outlet vapor quality.	90

Abstract

This Master thesis in Ingegneria Matematica is the result of a six months collaboration between the Dipartimento di Matematica of Politecnico di Milano and the ABB Switzerland Ltd Corporate Research Center of Baden, under the supervision of the principal scientists Francesco Agostini and Thomas Gradinger. The aim of this work is the computational modeling of a specific condenser as part of a two-phase thermosyphon power electronic cooling system.

The thesis is divided into the following five parts devoted to:

Part I: overview and comparison of three types of power electronics cooling devices and description of the specific thermosyphon cooler analyzed in this work;

Part II: mathematical modeling of the three physical coupled domains involved in the condenser device: external air, aluminum panel and two-phase refrigerant fluid;

Part III: description of suitable numerical approximation method for each domain involved in the computation, with emphasis on the stabilized methods used to deal with dominating convective flow regimes;

Part IV: discussion of the numerical results of the simulations for the two-phase condenser;

Part V: conclusive considerations and perspectives for future activities.

Riassunto della tesi

Introduzione

Il lavoro presentato in questa tesi è il risultato di una internship di sei mesi presso ABB Corporate Research Center di Baden, in Svizzera, sotto la supervisione e il supporto del Dipartimento di Matematica del Politecnico di Milano.

Lo scopo di questa collaborazione è la modellazione dal punto di vista matematico-fisico e la simulazione numerica di un particolare sistema di raffreddamento per componenti elettrici, ideato dai ricercatori ABB. Trattasi di un sistema di raffreddamento con struttura a termosifone che sfrutta l'elevato coefficiente di scambio termico dovuto all'utilizzo di fluidi bifase, ovvero fluidi presenti sia in fase liquida che in fase gassosa.

Nel Capitolo 1 forniremo prima una breve descrizione e confronto dei sistemi di raffreddamento utilizzati maggiormente nelle applicazioni industriali. In seguito, nella Sezione 1.2 descriveremo dettagliatamente la geometria e i fenomeni fisici coinvolti nel sistema di raffreddamento in questione. Potremo, infatti, interpretare la struttura del condensatore come l'unione di tre domini ben distinti, ma allo stesso modo in stretta comunicazione tra di loro: il flusso di aria esterna, i pannelli metallici e il fluido bifase che scorre nel canale.

Modelli Matematici

Il primo passo per l'analisi dei fenomeni fisici coinvolti è la derivazione di un modello matematico appropriato a descriverne le dinamiche. Questo compito verrà eseguito dominio per dominio nei tre capitoli della seconda parte di questo lavoro. Nel Capitolo 2, sotto opportune ipotesi, ricaveremo il modello matematico relativo

al flusso di aria esterno e tra i pannelli. Prenderemo in considerazione solo il caso di scambio di calore tramite convezione forzata, dove il flusso d'aria è imposto dall'esterno attraverso un ventilatore o soffiante. Nella Sezione 2.2.1 introdurremo il concetto di correlazione empirica e lo applicheremo al calcolo del coefficiente di scambio termico tra il dominio dell'aria e il pannello. In seguito, nella Sezione 2.2.2, descriveremo la tecnica per il calcolo della caduta di pressione del flusso di aria, parametro necessario per determinare la potenza minima della ventola utilizzata, introducendo il parametro detto *friction factor* e le corrispondenti correlazioni.

Nel Capitolo 3 ricaveremo il modello matematico per lo scambio di calore relativo alla parete metallica del pannello condensatore. Il pannello riceve il calore ceduto dal fluido bifase che si condensa, parte di esso è diffuso all'interno del pannello stesso e parte è disperso nell'aria.

Infine nel Capitolo 4, ricaveremo il modello termo-fluidodinamico del fluido bifase che scorre nel canale, considerando in primis l'ipotesi di incomprimibilità poi eliminata in seguito. Nella Sezione 4.2.1 introdurremo le relazioni costitutive necessarie per la descrizione delle proprietà termofisiche della miscela liquido-vapore considerata. Anche in questo caso dedichiamo l'intera Sezione 4.3 alla descrizione delle correlazioni utilizzate per il calcolo del coefficiente di scambio termico bifase e della perdita di pressione dovuta all'attrito tra fluido e parete del canale.

Metodi Numerici

Nella terza parte di questo lavoro introdurremo i metodi di discretizzazione appropriati per l'approssimazione numerica dei tre modelli descritti precedentemente.

Nel Capitolo 5 mostreremo una interpretazione dei modelli per i domini di aria e pannello come problemi bidimensionali di diffusione, trasporto e reazione. Per quanto riguarda la discretizzazione numerica proporrò un approccio ad elementi finiti misti, usando i metodi di stabilizzazione upwind e *fitting* esponenziale per i regimi a trasporto dominante.

Nel Capitolo 6 descriveremo un metodo di discretizzazione valido sia per la risoluzione delle equazioni di bilancio che per le relazioni costitutive del liquido bifase. Lo schema numerico descritto nel caso di fluido incomprimibile ha la particolarità di riuscire a configurare una arbitraria configurazione geometrica del canale, comprese le biforcazioni.

Infine nel Capitolo 7 analizzeremo le formulazioni algebriche corrispondenti ad ognuno dei tre problemi considerati, utilizzando un approccio di tipo *Nodal Analysis* per l'assemblaggio delle matrici relative al dominio fluido bifase. Proporre-

mo, inoltre, l'algoritmo iterativo utilizzato per risolvere le nonlinearità delle suddette formulazioni algebriche e la procedura di iterazione funzionale tra domini impiegata.

Risultati Numerici

Nel Capitolo 8 presenteremo ed analizzeremo una serie di risultati numerici ottenuti con il risolutore implementato. Mostriamo dapprima nella Sezione 8.1 i risultati ottenuti nel caso dei domini accoppiati di aria e pannello, confrontando i valori assunti dai due coefficienti di scambio termico coinvolti: tra aria e pannello e tra pannello e fluido bifase.

In seguito, nella Sezione 8.2.1 mostreremo i risultati ottenuti per il caso di fluido incomprimibile con una geometria del canale avente biforcazioni, mostrando la corrispondenza tra ogni segmento del canale e una specifica resistenza elettrica equivalente, pari alla resistenza idraulica.

Al contrario, i risultati ottenuti nel caso di fluido comprimibile e bifase verranno mostrati per un canale senza biforcazioni e utilizzando il fluido refrigerante R134a. Analizzeremo la variazione di *vapor quality* del fluido refrigerante in uscita dal canale in funzione della temperatura del pannello e della velocità del fluido, in modo da indagare sulle le condizioni iniziali di ottimalità.

Conclusioni

Nel capitolo conclusivo riassumiamo i principali risultati ottenuti in questo lavoro di tesi, evidenziando gli aspetti innovativi e i possibili futuri sviluppi di ricerca. Relativamente a questi ultimi, si individua l'esigenza di:

- includere il regime di trasporto a convezione naturale;
- rimuovere l'ipotesi di flusso bifase omogeneo;
- introdurre l'effetto delle cadute di pressione concentrate in corrispondenza di punti di curvatura o giunzione del canale.

Part I

Introduction

Description of an electronic cooling system and technological motivations

Since the early 1980s the growing of new technologies and applications shifted the scientific interest on the power electronics field. The necessity of industry to develop micro devices with a high heat dissipation per unit of volume justifies the need of more compact and high heat flux cooling systems.

In this thesis we will focus on the description, mathematical modeling and numerical discretization of a specific cooling system designed by the scientists of the ABB Corporate Research Center of Baden, Switzerland. The work presented is the result of a six-months internship in the mentioned research center, under the supervision and the support of the Department of Mathematics of Politecnico of Milano.

In this introductory chapter we will make a description and comparison of the most used power electronics cooling systems and a detailed description of the cooler analyzed in this work.

1.1 Cooling systems overview

Each power electronic device must be cooled to avoid excessive increase in temperature, which leads to failure of the device. Typically this kind of applications features high rates of heat generation and high power densities, hence making straightforward the necessity of developing optimal cooling systems.

All the cooling procedures exploit the convection heat transfer phenomenon, which occurs between a fluid in motion and a bounding surface when there is a gap of temperature between them. According to the *Newton's law of cooling* [IDW02, p. 8]

$$q = Ah(T_s - T_\infty), \quad (1.1)$$

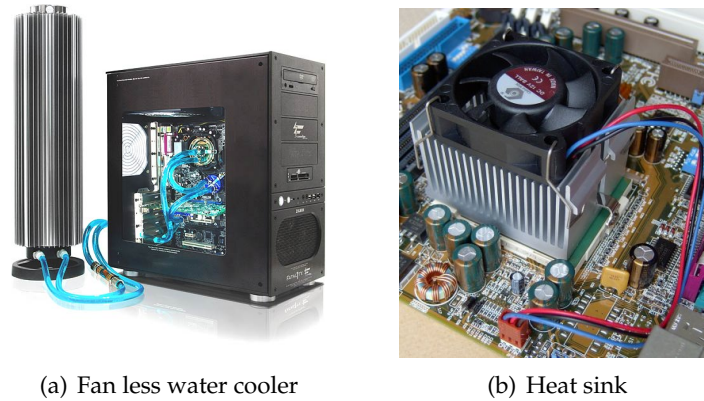


Figure 1.1: Examples of water and air-cooled electronic devices.

the convective heat power q is proportional to the difference between the surface and the fluid temperature, T_s and T_∞ respectively. The proportionally constant h is called *convection heat transfer coefficient* and A is the heat exchange surface.

There are different possibilities in the structure of cooling devices, the most used are presented below.

The water-cooled and air-cooled systems are the most exploited in power electronics applications, as shown in Figure 1.1 with an application of both systems to computer CPU cooling.

Water-coolers are used commonly for cooling combustion engines in automobiles and electrical generators. The water flowing in the pipes transports away the heat from the heat source to a secondary cooling surface. These systems are usually quite expensive because they need a moving pump that has a finite life and must be periodically serviced. The water cooling systems, compared to the air cooling systems, need less volumetric flow and reduced temperature differences for transmitting heat over greater distances, having higher specific heat capacity and thermal conductivity.

The convective air-cooled systems, called heat sink, consist of an array of fins, extended from a plate base connected to the electronic device, as in Figure 1.1(b). If a fan is used for increasing the air flow, the heat transfer phenomenon is due to forced convection and no longer to natural convection. The first purpose of the fin is to enhance the heat exchange surface, because, according to the law (1.1), at a fixed temperature difference the increase of surface A is proportional to the increase of heat flux. In fact, following this approach also the surface of each fin is enhanced by increasing the roughness of the surface, as shown in Figure 1.2. However, reducing the thickness and increasing at the same time the fin surface

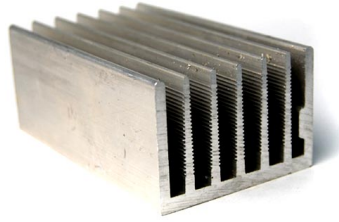


Figure 1.2: Example of an heat sink system.

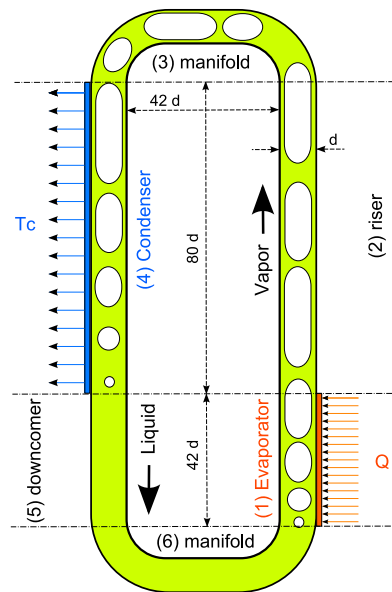


Figure 1.3: Thermosyphon.

we obtain a progressive reduction of the fin efficiency, due to the increase of variation of temperature in the extended surface.

The second purpose of the fin is to reduce the air cross section, in order to increase the air velocity and, consequently, the heat transfer coefficient.

To conclude this short review we analyze the two-phase cooler based on the thermosyphon criterion, described in Figure 1.3. As two-phase flow we denote a fluid where both liquid and vapor phases are present. The thermosyphon consists of an evaporator and a condenser connected by a pipe. The heat dissipated by electronic devices, in contact with the evaporator, is collected by means of an evaporating fluid. The vapor phase fluid, rising in the pipe, passes through the condenser where it returns to the liquid phase. No pumps are needed to move the refrigerant fluid from the evaporator to the condenser and in the way back, because this system takes advantage from the natural circulation of the inside two-phase fluid.

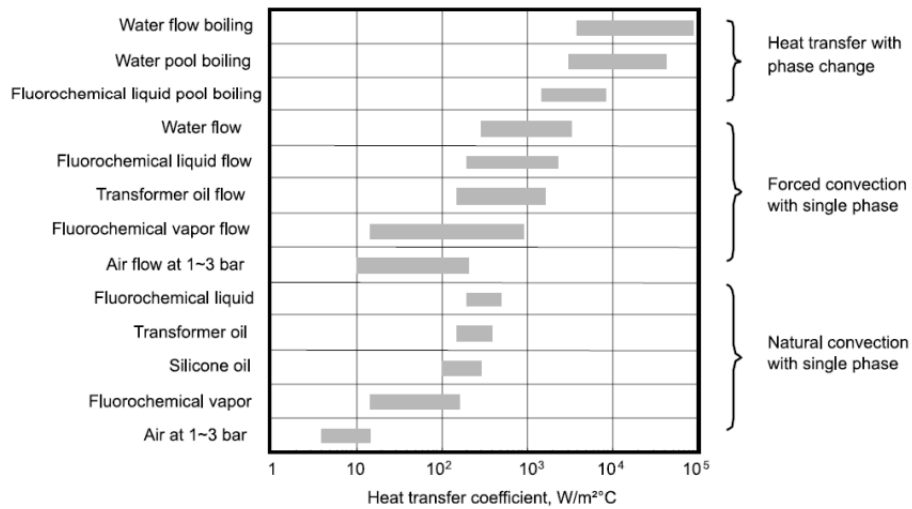


Figure 1.4: Comparison of the heat transfer coefficient values varying the cooling system.

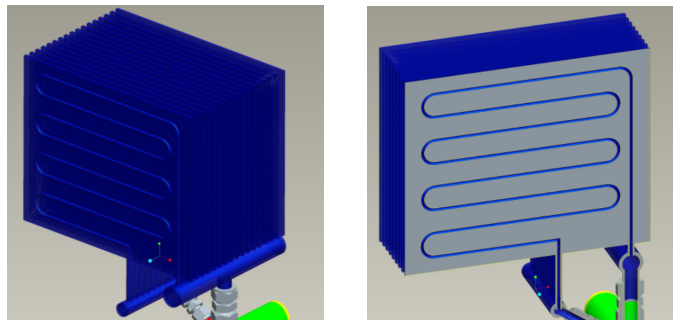


Figure 1.5: Geometry of the condenser.

The changing phase phenomena has a high thermodynamic efficiency: the two-phase fluid heat transfer coefficient value is significantly higher compared to the values corresponding to the medium fluids used in the cooling systems illustrated above, as shown in Figure 1.4, and the flow temperature is nearly constant due to the saturated nature of the liquid-vapor mixture.

1.2 A thermosiphon cooler

The cooling system designed by the scientist of the ABB Research Center is a two-phase thermosiphon cooler, whose condenser device is depicted in Figure 1.5. The evaporator, represented by the box at the bottom, and the condenser, represented by a series of panels, interact through two pipes: one for the vapor phase

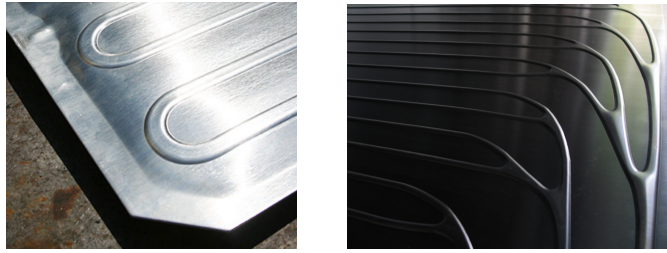


Figure 1.6: Examples of condenser panels.

raising from the evaporator to the condenser and one for the liquid phase which bring back the liquid at the evaporator inlet.

In this work we will focus on the description and analysis of the condenser device used in this particular example of thermosyphon cooler. From the geometrical point of view, the device is constituted of a series of aluminum panels connected in parallel to each other. Each panel consists of two aluminum plates bonded together for most of the surface, with the non bounded area being crossed by a channel, as depicted in Figure 1.6. The fluid flowing through the condenser panel is a refrigerant fluid.

We can consider now the thermo-physical phenomena occurring in this device. First of all we notice that there are three different physical domains involved: two-phase refrigerant fluid, aluminum panel and external air flow.

Two-phase refrigerant fluid. The refrigerant fluid at the inlet of the channel is almost totally vapor-phase. Flowing through the channel, it hands over heat to the panel metallic wall and returns to the liquid-phase. Figure 1.7 shows the main flow patterns assumed by the two-phase flow during the condensation. Each pattern corresponds to a specific distribution of the liquid and vapor phases in the channel, for details see [Wha96].

Aluminum panel wall. The panel wall is heated by the heat released by the refrigerant fluid flowing in the channel during the condensation process. This heat is spreaded in the panel wall itself and is handed over to the external air flow.

External air flow. The series of panels is subjected to an external air flow, that can be naturally caused by the difference of temperature between the air and the panels or imposed by an external device like a pump or a fan. An increased air flow velocity generally enhances the heat transfer between the heated aluminum panels and the external air.

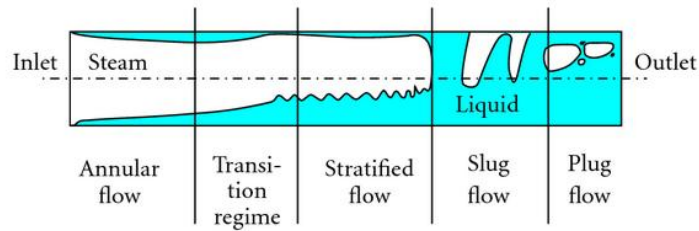


Figure 1.7: Two-phase flow patterns.

As described above the three physical domains are fully coupled, with the heat handed over by one of this domains corresponding to the heat received by an other domain.

Comparing this type of condenser to the air-cooled heat sink, we can notice that each panel acts as a fin, expanding the contact surface between the three domains. However, in this case the fin efficiency is close to one, because for any choice of panel dimension the aluminum temperature is more homogeneous, i.e. there is no significant temperature drop in the panel domain. This homogeneous distribution of temperature is the effect of the reduced panel thickness and of the high heat exchange between the panel and the two-phase fluid.

1.3 Technological motivations

The purpose of this collaboration project is to devise and implement a computational simulation solver for the condenser previously described. To fulfill this task, the first step is the mathematical modeling of the three thermo-physical problems involved, one for each domain mentioned previously. Consequently, we have to select and apply a suitable stable, conservative and accurate discretization method for each involved mathematical model. The last step is to end up with the proper computational routines for the numerical simulations.

The interest of the research scientists to develop this kind of simulator stems from the necessity of investigating the optimal configuration of this condenser, i.e the optimal geometry of the channel crossing the panels and the optimal input values of the air flow and of the two-phase refrigerant flow.

Part II

Mathematical Models

Description of the air subsystem

We will consider now the physical models for the description of the air subdomain. Assuming the same channel geometry and the same air flow condition for each panel, we can focus our study on the air domain included between two condenser panels.

Only the case of forced convection is considered in this work, which means that the air flow is imposed by an external pump or fan. In this case the air domain, that is physically three-dimensional, can be restricted to two dimensions; the heat exchange occurring in the thickness between two panels is neglected.

2.1 Air physical model

Let us consider the domain described in Figure 2.1. Ω is the three-dimensional domain embedded between two condenser panels located at $z = 0$ and $z = S$, respectively. Σ_w are the contact walls between air and panel, lying in the planes $z = 0$ and $z = S$ respectively. Σ_{in} and Σ_{out} are the inflow and outflow surfaces, lying in the planes $y = 0$ and $y = H$, respectively.

The model is derived under the assumptions of constant air density ρ , homogeneous flow, and constant average air speed v . The last assumption is the consequence of dealing with forced convection.

Only the three-dimensional energy balance equation must be solved

$$\partial_t(c_p \rho T) - \text{div}(k \nabla T - \rho c_p v T) = 0 \quad (x, y, z) \in \Omega, \quad (2.1)$$

with the boundary condition

$$-k \nabla T \cdot \mathbf{n} = h_{aw}(T - T_w) \quad (x, y, z) \in \Sigma_w. \quad (2.2)$$

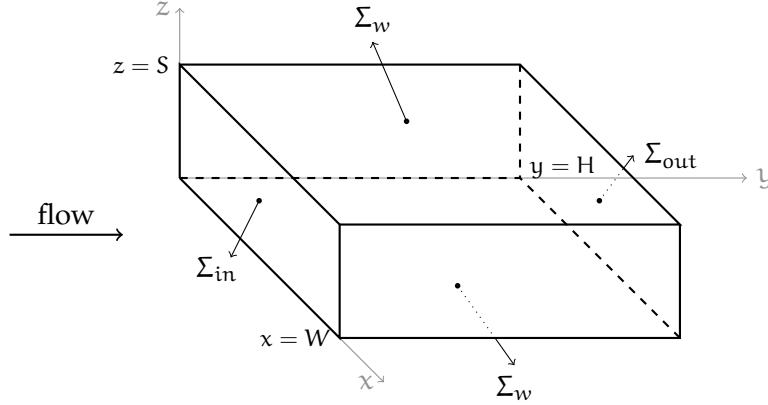


Figure 2.1: Air domain.

T is the air temperature, c_p is the air specific heat capacity at constant pressure and k is the thermal air conductivity. On the contact surfaces Σ_w the outflow heat flux is proportional to the difference between the air temperature T and the wall temperature T_w , through a coefficient h_{aw} accounting for the *heat transfer coefficient* between air and condenser wall. \mathbf{n} is the outward unit vector along the external surface of the domain.

Assuming equal conditions in the upper and lower contact surfaces Σ_w , we can define an adiabatic plane at $z = S/2$. Therefore, by symmetry, we can limit ourselves to consider only the domain between the adiabatic surface and one of the contact surfaces Σ_w , for example the one located at $z = 0$.

As previously mentioned, in the case of forced convection, we can neglect the heat transfer in the thickness between two panels, so we decide to use separation of variables to approximate the temperature distribution as

$$T(t, x, y, z) = \tilde{T}(t, x, y)\hat{T}(z). \quad (2.3)$$

$\tilde{T}(t, x, y)$ expresses the variation of temperature in the x, y plane, while $\hat{T}(z)$ is a dimensionless shape function accounting for the variation of temperature between the contact surface and the adiabatic plane located in $z = S/2$.

Integrating the energy balance equation in the vertical direction

$$\int_0^{S/2} [\partial_t(c_p \rho T) - \text{div}(k \nabla T - \rho c_p T \mathbf{v})] dz = 0$$

and using (2.3), we obtain

$$\left[\int_0^{S/2} \hat{T} dz \right] \partial_t (c_p \rho \tilde{T}) - \left[\int_0^{S/2} \hat{T} dz \right] \nabla_{x,y} \cdot (k \nabla_{x,y} \tilde{T} - \rho c_p \mathbf{v} \tilde{T}) - \tilde{T} \int_0^{S/2} \partial_z (k \partial_z \hat{T}) dz = 0. \quad (2.4)$$

Defining

$$\mathbb{I} = \int_0^{S/2} \partial_z (k \partial_z \hat{T}) dz,$$

we get

$$\mathbb{I} = \left[k \partial_z \hat{T} \right]_0^{S/2} = -k \partial_z \hat{T} \Big|_{z=0},$$

because $k \partial_z \hat{T} \Big|_{z=S/2} = 0$ under the assumption of adiabatic surface.

We can rewrite condition (2.2) as

$$-k \nabla T \cdot \mathbf{n} \Big|_{\Sigma_w} = k \tilde{T} \left(\partial_z \hat{T} \Big|_{z=0} \right) = h_{aw} \left(\tilde{T} \hat{T} \Big|_{z=0} - T_w \right).$$

Therefore the last term of equation (2.4) is equal to

$$\tilde{T} \mathbb{I} = -k \tilde{T} \left(\partial_z \hat{T} \Big|_{z=0} \right) = h_{aw} \left(T_w - \tilde{T} \hat{T} \Big|_{z=0} \right).$$

Defining now the parameter λ as

$$\lambda := \int_0^{S/2} \hat{T} dz, \quad (2.5)$$

equation (2.4) is

$$\lambda \partial_t (c_p \rho \tilde{T}) - \lambda \nabla_{x,y} \cdot (k \nabla_{x,y} \tilde{T} - \rho c_p \mathbf{v} \tilde{T}) - \tilde{T} \mathbb{I} = 0,$$

hence

$$\partial_t (c_p \rho \tilde{T}) - \nabla_{x,y} \cdot (k \nabla_{x,y} \tilde{T} - \rho c_p \mathbf{v} \tilde{T}) + \frac{h_{aw}}{\lambda} \left(\tilde{T} \hat{T} \Big|_{z=0} - T_w \right) = 0.$$

λ is the thickness of the thermal boundary layer at the interface between air and panel. It is a fitting parameter such that $\lambda \leq S/2$. We now rescale the shape function in such a way that $\hat{T} \Big|_{z=0} = 1$, this means that

$$T(t, x, y, 0) = \tilde{T}(t, x, y).$$

To ease the notation we will use the symbol T instead of \tilde{T} and set

$$\tilde{h}_{aw} = \frac{h_{aw}}{\lambda}.$$

In our model we neglect the development in transitional phase, focusing on the steady state solution, so that the physical model of the air phase reads

$$\left\{ \begin{array}{l} \nabla \cdot (-k\nabla T + \rho c_p \mathbf{v}T) + \tilde{h}_{aw}(T - T_w) = 0 \quad (x, y) \in (0, W) \times (0, H), \\ T = T_{in} \quad y = 0, \\ (-k\nabla T) \cdot \mathbf{n} = 0 \quad y = H, \\ (-k\nabla T + \rho c_p T) \cdot \mathbf{n} = 0 \quad x = 0, x = W. \end{array} \right. \quad (2.6)$$

The solution of the air domain problem (2.6) is coupled to the wall domain problem through the wall panel temperature T_w .

We have obtained that, neglecting heat exchanges through the air thickness between two condenser panels, the air domain is the planar intersection between the three-dimensional air area and the panel wall.

The first equation of system (2.6) is the divergence of the total heat flux per unit volume

$$\mathbf{q} = -k\nabla T + \rho c_p \mathbf{v}T,$$

this quantity is the sum of two contributions:

- conduction heat flux: $-k\nabla T$, according to the Fourier's law
- convection heat flux: $\rho c_p \mathbf{v}T$, proportional to the air velocity.

The boundary conditions associated with the air problem described in (2.6) are:

- Dirichlet boundary condition at the inflow boundary $y = 0$,
- null conduction heat flux at the outflow boundary $y = H$, i.e for $y > H$ the air flow is no more in contact with the panel surface,
- homogeneous Neumann condition on the remaining boundary.

It is important to notice that the air physical properties k and c_p are functions of the temperature, hence the system (2.6) is nonlinear.

2.2 Air correlations

To complete the description of the air domain model we have to provide a mathematical law for the heat transfer coefficient h_{aw} and introduce the *pressure drop* quantity.

We define an *empirical correlation* as a functional relation between two or more physical variables, usually validated by a series of experimental tests.

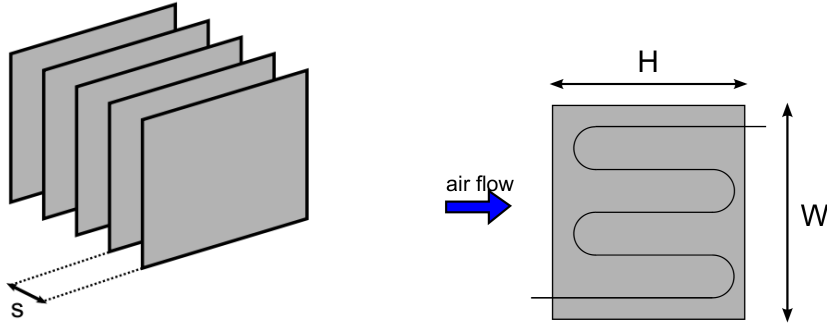


Figure 2.2: Geometry of the air problem.

In the engineering world, correlations are helpful to account of complex physical phenomena . There is a long list of correlations derived and studied in the literature, but each of them has a corresponding range of validity.

2.2.1 Air heat transfer coefficient correlation

The heat transfer coefficient can be expressed as a function of:

- *Prandtl number*: ratio of the kinematic viscosity ν and thermal diffusivity α

$$\mathbf{Pr} = \frac{\nu}{\alpha},$$

- *Reynolds number*: ratio of the inertia and viscous forces

$$\mathbf{Re} = \frac{|\mathbf{v}|L}{\nu},$$

where L is the characteristic length of the problem.

Notice that ν and α are, in general, parameters depending on the temperature of the medium. In the particular case of the heat flux between air and panel wall

$$h_{aw} = h_{aw}(T, \mathbf{Re}, \mathbf{Pr}).$$

Through empirical correlations the local *Nusselt number* \mathbf{Nu} is calculated as $\mathbf{Nu} = f(\mathbf{Re}, \mathbf{Pr})$ and is related to the heat transfer coefficient by the following formula:

$$h_{aw} = \frac{\mathbf{Nu} k}{L}.$$

The Nusselt number is a dimensionless parameter equal to the ratio of convective to conductive heat transfer across the exchange surface. We can also define the

average Nusselt number $\overline{\mathbf{Nu}}$, obtained integrating \mathbf{Nu} over the heat exchange surface.

In the case of the air domain defined in Figures 2.1 and 2.2, two different approaches can be used to derive the formula of \mathbf{Nu} .

First we can consider the air flow surrounding the panel as a flow on a flat plate at constant temperature, neglecting the roughness of the panel due to the projections of the channel. In this case the characteristic length L is equal to the size of the panel in the direction of the air flow H , so that the formula to calculate the Reynolds number becomes

$$\mathbf{Re}_H = \frac{|\mathbf{v}|H}{\nu}.$$

In the literature we can find several correlations for \mathbf{Nu} specifically developed for the case of flat plate. Few of the most well known correlations are here reported:

- flat plate correlation for laminar flow [IDW02, p. 393]

$$\mathbf{Nu}_H = 0.332\sqrt{\mathbf{Re}_H\mathbf{Pr}}^{1/3},$$

for $\mathbf{Re}_H \leq 10^4$ and $\mathbf{Pr} \geq 0.6$,

- Churchill-Ozoe for laminar flow [IDW02, p. 395]

$$\mathbf{Nu}_H = \frac{0.3387\mathbf{Re}_H^{1/2}\mathbf{Pr}^{1/3}}{[1 + (\frac{0.0468}{\mathbf{Pr}})^{2/3}]^{1/4}},$$

for $\mathbf{Re}_H \leq 10^4$ and $\mathbf{Re}_H\mathbf{Pr} \geq 100$,

- Chilton-Colburn for turbulent flow [IDW02, p. 395]

$$\mathbf{Nu}_H = 0.0296\mathbf{Re}_H^{4/5}\mathbf{Pr}^{1/3},$$

for $\mathbf{Re}_H \geq 10^4$ and $0.6 \leq \mathbf{Pr} \leq 60$.

As a second interpretation, we can consider the air flow through two panels as an intube flow. The correlations derived in the case of circular tubes can be adapted to tubes of each shape, using the *hydraulic diameter* D_h , defined as four times the flow cross sectional area divided by the *wet perimeter*

$$D_h = \frac{4WS}{2(W+S)}.$$

In this case the characteristic length $L = D_h$ and then

$$\mathbf{Re}_{D_h} = \frac{|\mathbf{v}|D_h}{\nu}.$$

Few of the most known correlations for \mathbf{Nu} in intube flow are:

- *Dittus-Boelter* for turbulent flow [IDW02, p. 491]

$$\mathbf{Nu}_{Dh} = 0.023\mathbf{Re}_{Dh}^{4/5}\mathbf{Pr}^n, \quad (2.7)$$

for $\mathbf{Re}_{Dh} \geq 10^4$, $0.7 \leq \mathbf{Pr} \leq 160$ and pipes long at least ten times Dh , $n = 0.4$ for heating and $n = 0.3$ for cooling,

- *Petukov* for turbulent flow [KSA87, Chap. 4]

$$\mathbf{Nu}_{Dh} = \frac{(f/8)\mathbf{Re}_{Dh}\mathbf{Pr}}{C + 12.7(f/8)^{1/2}(\mathbf{Pr}^{2/3} - 1)},$$

where

$$C = 1.07 + \frac{900}{\mathbf{Re}_{Dh}} - \frac{0.63}{1 + 10\mathbf{Pr}},$$

for $4000 \leq \mathbf{Re}_{Dh} \leq 5 \times 10^6$ and $0.5 \leq \mathbf{Pr} \leq 10^6$,

- *Gnielinski* for turbulent flow [KSA87, Chap. 4]

$$\mathbf{Nu}_{Dh} = \frac{(f/8)(\mathbf{Re}_{Dh} - 1000)\mathbf{Pr}}{1 + 12.7(f/8)^{1/2}(\mathbf{Pr}^{2/3} - 1)}$$

for $2300 \leq \mathbf{Re}_{Dh} \leq 5 \times 10^6$ and $0.5 \leq \mathbf{Pr} \leq 2000$.

f is the *friction factor*, a dimensionless parameter. A detailed description of this parameter will be provided in Section 2.2.2.

Entrance region correction

All of the previous cited intube flow correlations are suitable for *fully thermally developed flows*, hence far from the entrance region. If they are used in the *transition flow regions*, the convection coefficient is underestimated.

Bhatti and Shah propose [KSA87, Chap. 4] the following entrance region correction for the average Nusselt number $\overline{\mathbf{Nu}}$, calculated at the distance l from the entrance of the tube,

$$\frac{\overline{\mathbf{Nu}}}{\mathbf{Nu}_{fd}} = 1 + \frac{c}{(l/Dh)^m} \quad \text{if} \quad \frac{l}{Dh} > 3, \quad (2.8)$$

where \mathbf{Nu}_{fd} is the fully developed Nusselt number. The corresponding value of \mathbf{Nu}_{fd} is calculated using the intube correlations described above.

The values of the coefficients c and m depend on the entrance configurations [KSA87, Chap. 4]. The two configurations that are more similar to the air flow entrance region, Figure 2.3, are:

- long calming section: thermal boundary layer in the first part of the channel,

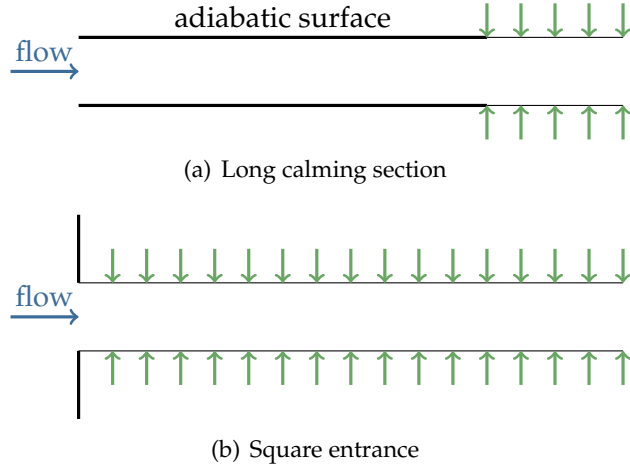


Figure 2.3: Two entrance region configurations. The black thick line denotes the adiabatic surface and the green arrows the heat exchanges.

configuration	c	m
long calming section	0.9756	0.76
square entrance	2.4254	0.676

Table 2.1: Values of the coefficients of the Bhatti and Shah entrance correction correlation, for the two cases considered.

- square entrance: flow contraction at the inflow entrance.

We decide to use an arithmetic mean of the fully developed Nusselt number \overline{Nu} calculated in the two mentioned configurations, the respective values of the coefficients are summarized in Table 2.1.

2.2.2 Pressure drop

In the solution of the air domain problem we are interested in the value of the pressure drop, because this parameter determines pump or fan power requirements. The air pressure drop can be post-calculated once system (2.6) has been solved [IDW02, p. 470]. We first introduce the *Moody friction factor*

$$f = -\frac{(dp/dx)Dh}{\rho v^2/2},$$

this parameter is dimensionless and assumes constant values in the fully developed regions. This parameter must not be confused with the *friction coefficient* C_f :

	A	B	m
$\mathbf{Re}_{Dh} < 2100$	0	16	1
$2100 \leq \mathbf{Re}_{Dh} \leq 4000$	0.0054	2.3×10^6	-2/3
$4000 < \mathbf{Re}_{Dh}$	1.28×10^{-3}	0.1143	3.2154

Table 2.2: Bhatti and Shah friction factor correlation coefficients.

the relation between the two parameters is $C_f = f/4$.

Using the definition of f , the pressure drop Δp for a fully developed flow from the axial position x_1 to x_2 , along the flow direction, can be expressed as

$$\Delta p = - \int_{p_1}^{p_2} dp = f \frac{\rho v^2}{2Dh} \int_{x_1}^{x_2} dx = f \frac{\rho v^2}{2Dh} (x_2 - x_1). \quad (2.9)$$

This is valid under the assumption of constant pressure gradient dp/dx , which is approximately true if we consider a small enough gap between x_1 and x_2 .

The pump power required to overcome the resistance to the flow can be calculated as

$$P = \Delta p \frac{\dot{m}}{\rho}$$

where \dot{m}/ρ is the mass flow rate.

Friction factor

The values of this dimensionless parameter can be calculated through empirical correlations. Few well known correlations available in literature are here reported:

- *Petukov* for turbulent flow [KSA87, Chap. 4]

$$f = (0.79 \ln(\mathbf{Re}_{Dh}) - 1.64)^{-1},$$

for $3000 \leq \mathbf{Re}_{Dh} \leq 5 \times 10^6$

- *Bhatti and Shah* for turbulent flow [KSA87, Chap. 4]

$$f = 4C_f = 4 \left(A + \frac{B}{(\mathbf{Re}_{Dh})^{1/m}} \right), \quad (2.10)$$

for the values of the coefficients A , B and m , see Table 2.2.

Description of the panel subsystem

In this chapter we will describe the physical model of the panel wall domain. The model will account for the distribution of the temperature in the panel, due to the diffusion heat flux in the aluminum wall. The heat sources are due to the heat flux between the two-phase flow and the panel and between the panel and the external air flow. The panel wall acts as an intermediary. In the zones where the panel is crossed by the channel, it receives the heat handed over by the cooling fluid through convection. Then this heat is spread in the panel itself by conduction and is handed over through convection to the air.

3.1 Panel physical model

To derive the two-dimensional model, we start from the three-dimensional energy balance equation

$$\partial_t(\rho c_p T) + \operatorname{div}(-k \nabla T) = 0 \quad \text{in } \Omega, \quad (3.1)$$

associated with the condition

$$-k \nabla T \cdot \mathbf{n} = h_{aw}(T - T_a) \quad \text{on } \Sigma_e. \quad (3.2)$$

Σ_e are the contact surfaces between the panel and the air in Figure 3.1.

Since the size in the z direction is negligible compared to the size of the panel in the other directions, we can neglect the heat transfer in the thickness S of the panel. Using the same approach described in Section 2.1, we assume

$$T(t, x, y, z) = \tilde{T}(t, x, y) \hat{T}(z).$$

The plane $z = S/2$ is a plane of symmetry for the panel domain problem, hence we can limit ourselves to consider only one of the regions separated by such a plane,

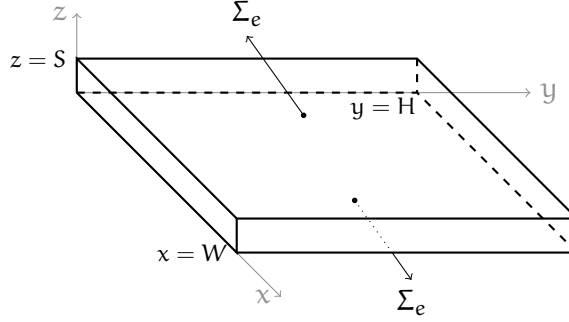


Figure 3.1: Panel domain.

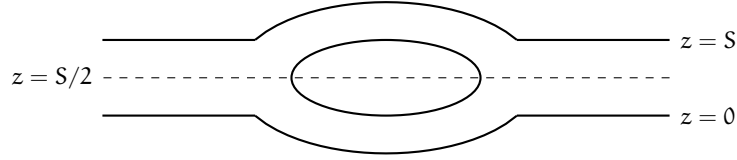


Figure 3.2: Thickness of the panel. The concavities on the panel surfaces coincide with the zones crossed by the channel. The dashed line denotes the plane of symmetry.

Figure 3.2.

If we call Λ the surface of the domain in the plane $z = S/2$, Λ can be divided in two different regions: Λ_c is the part of the surface crossed by the channel and Λ_a is such that $\Lambda_a \cap \Lambda_c = \emptyset$ and $\Lambda_a \cup \Lambda_c = \Lambda$. An example of this partitioning procedure is illustrated in Figure 3.3.

In this case the term \mathbb{I} , following the same procedure used in the case of the air domain, is equal to

$$\mathbb{I} = \left[k \partial_z \hat{T} \right]_0^{S/2},$$

so that we have

$$-k \partial_z \hat{T} \Big|_{z=0} = h_{aw} \left(\hat{T} \Big|_{z=0} - T_w \right)$$

and

$$k \partial_z \hat{T} \Big|_{z=S/2} = \begin{cases} 0 & \text{if } (x, y) \in \Lambda_a, \\ h_{wc} \left(\hat{T} \Big|_{z=S/2} - T_c \right) & \text{if } (x, y) \in \Lambda_c, \end{cases}$$

where T_c is the fluid temperature. This means that we have an adiabatic condition on Λ_a , while the input heat steam on Λ_c is equal to the heat handed over by the fluid.

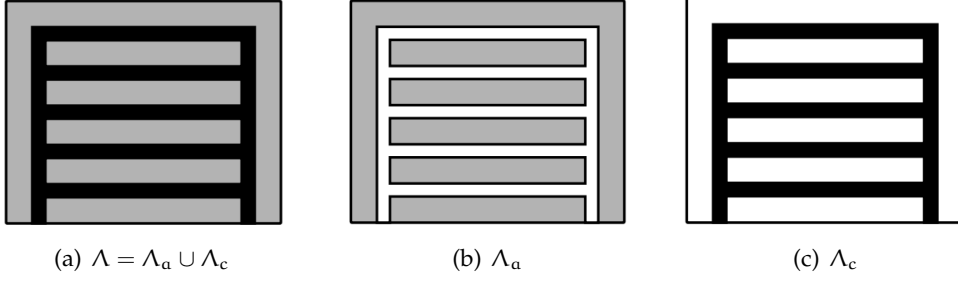


Figure 3.3: An example of partition of surface Λ .

From the above assumptions we can rewrite the energy equation as

$$\partial_t(c_p \rho \tilde{T}) - \nabla_{x,y} \cdot (k \nabla_{x,y} \tilde{T}) + \frac{h_{aw}}{\lambda} (\tilde{T} \hat{T}|_{z=0} - T_a) + \frac{h_{wc}}{\lambda} (\tilde{T} \hat{T}|_{z=S/2} - T_c) = 0.$$

where we assumed $h_{wc} = 0$ on Λ_a . Neglecting the heat transfer in the panel thickness, as previously described, we can consider \hat{T} constant and rescale it to be equal to one.

To simplify the notation we will use the symbol T to denote \tilde{T} and we introduce

$$\tilde{h}_{aw} = \frac{h_{aw}}{\lambda} \quad \text{and} \quad \tilde{h}_{wc} = \frac{h_{wc}}{\lambda},$$

where λ is defined as in (2.5). The two-dimensional steady state problem for the panel domain is

$$\begin{cases} \nabla \cdot (-k \nabla T) + \tilde{h}_{aw}(T - T_a) + \tilde{h}_{wc}(T - T_c) = 0 & (x, y) \in \Omega_w, \\ -k \nabla T \cdot \mathbf{n} = 0 & (x, y) \in \partial \Omega_w, \end{cases} \quad (3.3)$$

where $\Omega_w = (0, W) \times (0, H)$.

The associated boundary conditions are homogeneous Neumann, this means that the edges of the panel are perfectly isolated, hence the total outgoing heat flux is null. System (3.3) is coupled to the air and channel models through the air temperature T_a and the channel temperature T_c .

The heat transfer coefficient h_{wc} is zero in the plate zone where the panel wall is not crossed by the channel, otherwise it is calculated using the two-phase correlations that we will describe in the following chapter. The heat transfer coefficient h_{aw} is calculated using single-phase correlations as described in Section 2.2.1.

Description of the channel subsystem

In this chapter we will focus on the study of the motion of the two-phase fluid in the condenser channel. We will deduce the model to describe the problem according to a physical procedure of increasing complexity. The first considered model is under the assumption of incompressible and homogeneous flow of a single phase fluid. Then we will introduce the compressible flow assumption and the two-phase constitutive relations.

4.1 Single-phase incompressible fluid

The first physical model analyzed will assume incompressible flow, i.e constant density. We denote by \mathbf{v} the vector of the fluid velocity and by ρ the fluid density and as a starting point we will focus on the motion in a horizontal channel. As a second step we will introduce the gravity acceleration effect in a vertical channel.

4.1.1 Horizontal channel

We consider the domain shown in Figure 4.1, where L is the length of the trunk of channel, Σ is the channel cross section surface, Σ_e is the external surface and \mathbf{n} is the outward unit normal vector along Σ_e .

The three-dimensional physical model is deduced from the conservative form of the *Navier-Stokes* equations:

$$\begin{cases} \rho \operatorname{div}(\mathbf{v}) = 0 \\ \operatorname{div}(-\mu \nabla \mathbf{v} + \rho \mathbf{v} \otimes \mathbf{v}) + \nabla p = 0 \\ \operatorname{div}(-k \nabla \mathbf{T} + \rho \mathbf{v} h) = 0 \end{cases} \quad (x, y, z) \in \Omega, \quad (4.1)$$

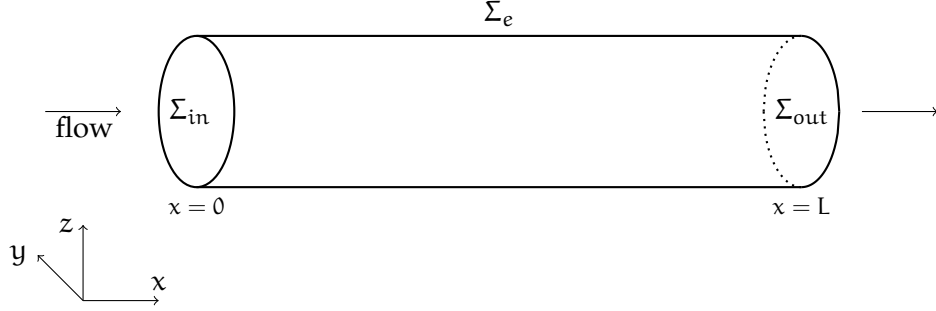


Figure 4.1: Horizontal channel domain.

i.e. the mass, momentum and energy balance equations. The specific enthalpy h is

$$h = \left(c_v T + \frac{1}{\rho} p \right).$$

No-slip boundary conditions are imposed on the external surface

$$\mathbf{v} = 0 \quad (x, y, z) \in \Sigma_e$$

and

$$-k \nabla T \cdot \mathbf{n} = h_{wc} (T - T_w) \quad (x, y, z) \in \Sigma_e,$$

i.e. the outflow component of the diffusion heat flux is equal to a source energy contribution, due to the temperature difference between the fluid temperature T and the panel wall temperature T_w . h_{wc} is the heat transfer coefficient between the panel wall and the fluid. We introduce the symbols μ for the fluid dynamic viscosity, k for the fluid thermal conductivity and c_v for the specific heat capacity at constant volume.

We now describe the approximations needed to pass from the three-dimensional model to a one-dimensional model along the x coordinate, parallel to the direction of the channel. The componentwise version of system (4.1) is

$$\left\{ \begin{array}{l} \rho \operatorname{div}(\mathbf{v}) = 0 \\ \operatorname{div}(-\mu \nabla v_x + \rho v_x \mathbf{v}) + \partial_x p = 0 \\ \operatorname{div}(-\mu \nabla v_y + \rho v_y \mathbf{v}) + \partial_y p = 0 \\ \operatorname{div}(-\mu \nabla v_z + \rho v_z \mathbf{v}) + \partial_z p = 0 \\ \operatorname{div} \left(-k \nabla T + \rho \mathbf{v} \left(c_v T + \frac{1}{\rho} p \right) \right) = 0 \end{array} \right. \quad (x, y, z) \in \Omega. \quad (4.2)$$

Assuming that the velocity is only in the x direction

$$\mathbf{v} = \begin{bmatrix} v_x \\ 0 \\ 0 \end{bmatrix},$$

the mass balance equation becomes

$$\rho \operatorname{div}(\mathbf{v}_x) = \partial_x v_x = 0,$$

so we deduce that $v_x = v_x(\mathbf{y}, z)$: the velocity in the x direction is constant but it changes in the channel cross section. We introduce the mean of v_x in the channel cross section surface

$$\langle v \rangle := \frac{1}{|\Sigma|} \int_{\Sigma} v_x \, dy \, dz$$

and we integrate the mass balance equation on Σ , to obtain

$$\int_{\Sigma} \rho \partial_x v_x \, dy \, dz = \rho \partial_x (|\Sigma| \langle v \rangle) = 0$$

from which we can introduce the new variable \dot{m} , flux of mass, defined as

$$\rho |\Sigma| \langle v \rangle = \text{const} = \dot{m}.$$

The three scalar components of the momentum equations become

$$\begin{cases} -\mu(\partial_y^2 + \partial_z^2)v_x + \partial_x p = 0, \\ \partial_y p = 0, \\ \partial_z p = 0, \end{cases}$$

from which we deduce that the pressure of the fluid is constant over the cross section of the pipe, $p = p(x)$.

Since $v_x = v_x(\mathbf{y}, z)$, there exists a constant value K such that

$$\begin{cases} \partial_x p(x) = -K, \\ -\mu(\partial_y^2 + \partial_z^2)v_x(\mathbf{y}, z) = K. \end{cases}$$

The solution of the problem

$$\begin{cases} -\mu(\partial_y^2 + \partial_z^2)v_x(\mathbf{y}, z) = K & \text{in } \Omega, \\ v_x = 0 & \text{on } \Sigma_e \end{cases}$$

is

$$K = R(\Sigma, \mu, \rho) \dot{m},$$

accordingly we deduce that

$$\partial_x p = -R(\Sigma, \mu, \rho) \dot{m}. \quad (4.3)$$

The function $R(\Sigma, \mu, \rho)$ is the *hydraulic resistance* of the pipe to the mass flow. In the case of a pipe with circular cross section of radius r the following relation holds

$$R(\Sigma, \mu, \rho) = \frac{8\mu}{\rho\pi r^4},$$

hence \dot{m} is proportional to the fourth power of r , for details see [LL87, p. 51].

Finally we can analyze the energy balance equation.

We split the divergence operator in the two main directions of the problem:

- $(\cdot)_{\parallel}$ denotes the restriction of the operator in the direction parallel to the channel, that is x ,
- $(\cdot)_{\perp}$ denotes the restriction in the plane perpendicular to the channel, that is the plane yz .

Integrating along the surface Σ we obtain

$$\begin{aligned} \int_{\Sigma} \operatorname{div}_{\parallel} \left[-k\nabla_{\parallel} T + \rho v \left(c_v T + \frac{1}{\rho} p \right) \right] dy dz + \int_{\Sigma} \operatorname{div}_{\perp} (-k\nabla_{\perp} T) dy dz &= \\ \operatorname{div}_{\parallel} \left[-k\nabla_{\parallel} \int_{\Sigma} T dy dz + \int_{\Sigma} \rho v \left(c_v T + \frac{1}{\rho} p \right) dy dz \right] + \int_{\partial\Sigma} -k\nabla_{\perp} T \cdot \mathbf{n} d\sigma &\simeq \\ \operatorname{div}_{\parallel} \left[-k|\Sigma| \nabla_{\parallel} \langle T \rangle + \dot{m} \left(c_v \langle T \rangle + \frac{1}{\rho} p \right) \right] + |\partial\Sigma| h_{wc} (\langle T \rangle - T_w) &= 0 \end{aligned}$$

where we have defined the average temperature

$$\langle T \rangle := \frac{1}{|\Sigma|} \int_{\Sigma} T dy dz,$$

quantity constant in each surface Σ , and we have assumed $T \simeq \langle T \rangle$ on each cross section surface and on $\partial\Sigma$.

Since the direction parallel to the motion is x , the energy balance equation obtained for the one-dimensional approximate problem is

$$\partial_x \left(-k|\Sigma| \rho \partial_x \langle T \rangle + \dot{m} \rho c_v \langle T \rangle + \dot{m} p \right) + |\partial\Sigma| \rho h_{wc} (\langle T \rangle - T_w) = 0,$$

that can be rewritten as

$$\partial_x (-\alpha \partial_x T + \beta T + \dot{m} p) + \gamma (T - T_w) = 0$$

upon introducing the parameters

$$\begin{cases} \alpha &= k\rho|\Sigma|, \\ \beta &= \dot{m}\rho c_v, \\ \gamma &= |\partial\Sigma|\rho h_{wc}. \end{cases}$$

With a slight abuse of notation, we will use the symbol T instead of $\langle T \rangle$.

In conclusion, starting from the three-dimensional problem (4.2) we have derived the following one-dimensional physical model to simulate the motion of an incompressible, homogeneous and single-phase fluid in a horizontal channel

$$\begin{cases} \partial_x p + R(\Sigma, \mu, \rho)\dot{m} &= 0 \\ \partial_x (-\alpha\partial_x T + \beta T + \dot{m}p) + \gamma(T - T_w) &= 0 \end{cases} \quad x \in (0, L), \quad (4.4)$$

where $\dot{m} = \text{const.}$ The equations in system (4.4) are uncoupled so that the first equation can be solved first, and the computed pressure p can be plugged in the second equation that becomes a diffusion, advection and reaction equation for the dependent variable T .

The natural boundary conditions associated with problem (4.4) are

$$\begin{cases} p &= p_{\text{in}} & x = 0, \\ T &= T_{\text{in}} & x = 0, \\ -\alpha\partial_x T &= 0 & x = L, \end{cases}$$

i.e. Dirichlet conditions for T and p at the inlet, and Neumann conditions at the outlet boundary. We impose that the outlet heat flux is only equal to the convection contribution, hence the diffusion contribution is equal to zero, this is equivalent to assuming that the contact between the fluid and the heated channel wall ends after $x = L$. The value of \dot{m} is an input datum of the problem.

4.1.2 Vertical channel

We discuss now the changes to be applied to the model (4.4) in the case of a vertical trunk of channel, like in Figure 4.2.

The three-dimensional Navier-Stokes equations in conservative form are:

$$\begin{cases} \rho \operatorname{div}(\mathbf{v}) &= 0 \\ \operatorname{div}(-\mu\nabla\mathbf{v} + \rho\mathbf{v} \otimes \mathbf{v}) + \nabla p &= \rho\mathbf{g} \\ \operatorname{div}(-k\nabla T + \rho\mathbf{v}h) &= 0 \end{cases} \quad (x, y, z) \in \Omega, \quad (4.5)$$

where \mathbf{g} is the acceleration of gravity vector

$$\mathbf{g} = \begin{bmatrix} 0 \\ 0 \\ -g_z \end{bmatrix}.$$

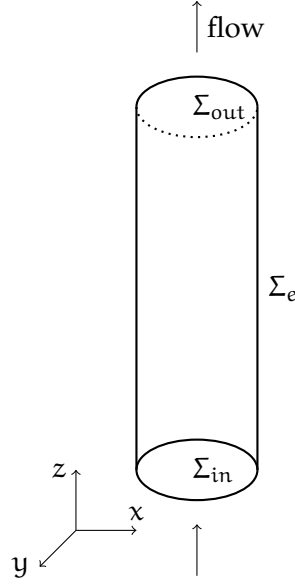


Figure 4.2: Vertical channel domain.

The associated boundary conditions are, as in the horizontal case, given by

$$\begin{cases} \mathbf{v} = 0 \\ -k\nabla T \cdot \mathbf{n} = h_{wc}(T - T_w) \end{cases} \quad (x, y, z) \in \Sigma_e. \quad (4.6)$$

Compared to the horizontal case, the specific enthalpy in the vertical case has an additional term due to the gravity effect, proportional to the coordinate z

$$h = \left(c_v T + \frac{1}{\rho} p + g_z z \right).$$

The componentwise form of (4.5) becomes now

$$\begin{cases} \rho \operatorname{div}(\mathbf{v}) = 0 \\ \operatorname{div}(-\mu \nabla v_x + \rho v_x \mathbf{v}) + \partial_x p = 0 \\ \operatorname{div}(-\mu \nabla v_y + \rho v_y \mathbf{v}) + \partial_y p = 0 \\ \operatorname{div}(-\mu \nabla v_z + \rho v_z \mathbf{v}) + \partial_z p = -\rho g_z \\ \operatorname{div} \left(-k \nabla T + \rho \mathbf{v} \left(c_v T + \frac{1}{\rho} p + g_z z \right) \right) = 0 \end{cases} \quad (x, y, z) \in \Omega. \quad (4.7)$$

The signs of the contributions due to the gravity acceleration refer to the domain in Figure 4.2, where z and \mathbf{g} have an opposite orientation.

Assuming that

$$\mathbf{v} = \begin{bmatrix} 0 \\ 0 \\ v_z \end{bmatrix}$$

and applying to system (4.7) the same approach described in the previous section, we obtain the following one-dimensional physical problem for the vertical channel:

$$\begin{cases} \partial_z p + R(\Sigma, \mu, \rho) \dot{m} + \rho g_z = 0 \\ \partial_z (-\alpha \partial_z T + \beta T + \dot{m}(p + \rho g_z z)) + \gamma(T - T_w) = 0 \end{cases} \quad z \in (0, L). \quad (4.8)$$

The two unknown variables are the pressure p and the temperature T . The appropriate boundary conditions for (4.8) are

$$\begin{cases} p = p_{\text{in}} & z = 0, \\ T = T_{\text{in}} & z = 0, \\ -\alpha \partial_z T = 0 & z = L. \end{cases}$$

4.2 Two-phase compressible fluid

We consider now the physical model of the fluid motion removing the assumption of incompressible flow, so the density ρ is no more constant.

Starting from the three-dimensional Navier-Stokes equations and following the same steps of the Sections 4.1.1 and 4.1.2, we get the one-dimensional problem

$$\begin{cases} \partial_x G_x = 0 \\ \partial_x (G_x v_x) + \partial_x p = f_x \\ \partial_x (h G_x) + |\partial \Sigma| h_{wc} (T - T_w) = 0 \end{cases} \quad x \in (0, L), \quad (4.9)$$

where x is the direction of the flow and we have defined $G_x = \rho v_x$. The quantity that is constant in the evolution of the motion is no more v_x , because ρ is no more constant, but G_x . The model is derived under the assumption of neglecting the diffusion contribution in the energy balance equation. We notice that in the momentum equation the viscous term depending on the parameter μ is included in the right hand side.

Problem (4.9) has three equations for five dependent variables v_x , G_x , T , p and h , so that the solution of the problem is not uniquely determined and it is necessary to add at least two constitutive equations.

Compared to the incompressible case, the mathematical expression of f_x is no more easily obtainable, but we need to use specified two-phase flow correlations. This is necessary also for the two-phase expression of h and ρ .

System (4.9) is a general formulation of the problem valid in both cases of horizontal and vertical channels, the difference being an extra term in f_x in the constitutive relation for h . The associated boundary conditions are of Dirichlet type at the in-flow boundary because (4.9) is a system of hyperbolic equations.

4.2.1 Two-phase liquid-vapor flow

We have to consider now that in the condenser channel a liquid-vapor mixture of the same refrigerant fluid is present.

To describe the mixture of the two phases we introduce two significant quantities.

Vapor quality:

$$x = \frac{m_v}{m_v + m_L},$$

a dimensionless variable equal to the rate of vapor phase mass m_v and respect to the total mass flowing in the pipe. The subscript $(\cdot)_V$ denotes the quantity of the vapor-phase, likewise the subscript $(\cdot)_L$ refers to the liquid-phase of the fluid,

Void fraction:

$$\varepsilon = \frac{V_V}{V_V + V_L},$$

where V_V is the volume of channel occupied by the vapor-phase and V_L is the corresponding volume occupied by for the liquid-phase.

To clarify the difference between ε and x , consider a bottle half full of a liquid and the remaining part occupied by its vapor. If we assume that the density ratio of liquid is 5 : 1, then the vapor quality x is equal to 1/6, while, regardless of the density of the liquid or vapor in the bottle, the void fraction is always equal to 1/2. To describe the thermo-physical dynamics of the two-phase flow, we need to add x and ε to the unknowns variables T , p , v and h .

In order to end up with a closed system of equations, we have to add the two-phase constitutive relations

$$\begin{cases} \rho = \rho(\varepsilon, T) = \rho_L(1 - \varepsilon) + \rho_V\varepsilon, \\ h = h(x, T) = h_L(1 - x) + h_Vx, \\ \varepsilon = \varepsilon(x, T), \\ p = p(T), \end{cases} \quad (4.10)$$

to the three conservation equations (4.9).

The two-phase density ρ and enthalpy h are calculated through the empirical interpolation between all liquid flow and all vapor flow quantities. The single phase values are respectively weighted by the void fraction or by the vapor quality. We remark that all the single-phase quantities for liquid or vapor flow depend implicitly on the temperature T , hence system (4.10) is nonlinear. The void fraction is expressed through an empirical correlation, for example, one of the most popular

in the case of horizontal channels is the *Rouhani-Axelsson* [RA70]. We assume that, during the change of phase, the development of temperature follows the saturation curve, hence the pressure depends only on the temperature and vice versa. For a detailed description of the two-phase constitutive relations, we refer to [CT96], [Tho06] and [Wha96].

Homogeneous model

In this thesis we consider the special case of a *homogeneous two-phase model*, under the assumption of the two phases traveling with the same velocity. In this case there is an explicit formula for the homogeneous void fraction

$$\varepsilon = \frac{x/\rho_V}{(1-x)/\rho_L + x/\rho_V},$$

which allows us to eliminate one equation from system (4.10) and to express ρ as a weighted average of ρ_L and ρ_V through x . The variable ε can then be eliminated from the variable set, to obtain the following homogeneous two-phase constitutive relations

$$\begin{cases} \rho &= \frac{\rho_V \rho_L}{\rho_V(1-x) + \rho_L x}, \\ h &= h_L(1-x) + h_V x, \\ p &= p(T). \end{cases} \quad (4.11)$$

Henceforth, when we will refer to the two-phase constitutive relations we will always consider system (4.11).

4.3 Two-phase flow correlations

As we have done for air and panel, we dedicate a section to the description of the empirical correlations used in two phase flow. This expression will be for the heat transfer coefficient h_{vc} and for the pressure drop.

The choice of suitable correlations in the case of a two-phase flow is quite more complicated than for a single-phase flow, because the range of validity of the correlations depends on the flow patterns of the cooling flow. Ideally, one should use a different correlation for each part of the pipe.

4.3.1 Two-phase heat transfer coefficient correlation

After analyzing the review of the most recent correlation of the heat transfer coefficient for condensation inside tubes [CCDC⁺03] and [GV03], we have decided to

use the *Shah* correlation [Sha79] valid for film condensation pattern. According to Shah the heat transfer coefficient can be expressed as

$$h_{wc} = h_{wcL} \left[(1-x)^{0.8} + \frac{3.8x^{0.76}(1-x)^{0.04}}{p_r^{0.38}} \right] \quad \text{for } x < 0.85, \quad (4.12)$$

where h_{wcL} is the condensing heat transfer coefficient assuming the liquid phase flowing alone in the tube. This value is approximated with single-phase correlations, see as reference Section 2.2.1. The symbol p_r denotes the reduced pressure, equal to

$$p_r = \frac{p}{p_c},$$

where p_c is the pressure at the critical point. The value p_c is a function of the fluid type, for example in the case of the refrigerant fluid R134a is equal to 4.06MPa. The critical point is the point above which the liquid phase of the material ceases to exist.

This correlation is valid for both cases of horizontal and vertical pipes. The trend of the expression (4.12) is such as for $x = 0$ the two-phase coefficient converges to the corresponding single phase one. Instead for $x = 1$, value out of the validated range of $x < 0.85$, the predicted values of h_{wc} converge abruptly to zero.

We propose a modified Shah correlation

$$\widehat{h_{wc}} = h_{wc} + x^\alpha h_{wcV}, \quad (4.13)$$

in such a way that for $x = 1$ we have $\widehat{h_{wc}} = h_{wcV}$. The values of the coefficient α modulate the weight of h_{wcV} in the formula. Decreasing the value of α we increase the weight of the term h_{wcV} in the formula (4.13) and the difference between h_{wc} and $\widehat{h_{wc}}$ in the range $x > 0.8$, as shown in Figure 4.3.

4.3.2 Pressure drop

Considering now the momentum conservation equation

$$\text{div}(\rho v_x^2) + \partial_x p + \rho g_z = f_x,$$

we have to investigate the expression at the right hand side.

Consulting the works focused on the study of multiphase flow [QT05, Chap. 4] and [Tho06, Chap. 13], we find the following expression for the total pressure drop

$$\Delta p = \Delta p_m + \Delta p_s + \Delta p_f,$$

consisting of the sum of three terms: the momentum pressure drop, static pressure drop and frictional pressure drop.

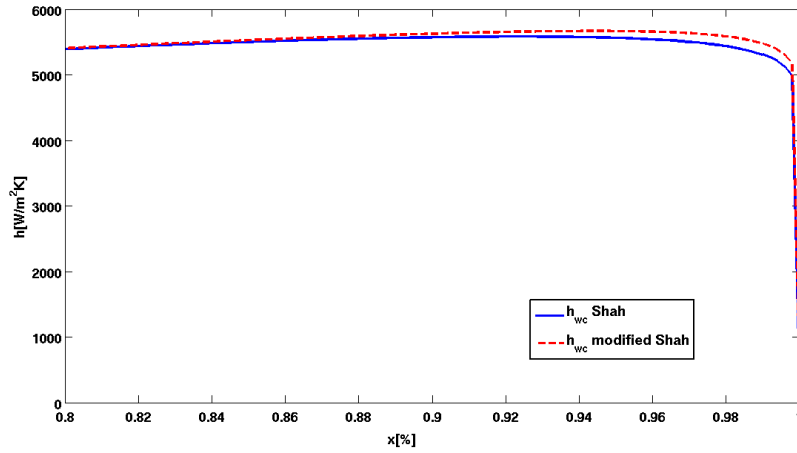


Figure 4.3: Trend of the Shah correlation (4.12) in blue and of the modified correlation (4.13) in red and dashed line, with $\alpha = 12$ and in the range $0.8 < x < 1$. R134a refrigerant fluid at temperature of 60°C and velocity of 0.6m/s flowing in a circular pipe of radius 0.6cm . The single-phase heat transfer coefficients h_{wcL} and h_{wcV} are calculated through the Dittus-Boelter correlation.

There is a perfect match between the two equations, with the following correspondence between the terms

- total pressure drop:

$$\Delta p \rightarrow \partial_x p,$$

- momentum pressure drop: reflects the changes in the kinetic energy

$$\Delta p_m \rightarrow -\text{div}(\rho v_x^2),$$

- static pressure drop: reflects the changes in the potential energy

$$\Delta p_s \rightarrow -\rho g_z,$$

- frictional pressure drop: due to the friction on the channel wall

$$\Delta p_f \rightarrow f_x.$$

Hence f_x can be expressed through a specific empirical correlation for the frictional pressure drop. According to [MSH86] the *Müller-Steinhagen and Heck* frictional pressure gradient correlation is the most convenient to use in general.

Under the assumption of a homogeneous model, the frictional pressure gradient can be expressed as

$$\Delta p_f = \frac{2C_f \rho |v_x|^2}{Dh},$$

where the friction coefficient is expressed by the *Blasius equation*

$$C_f = \frac{0.079}{\mathbf{Re}^{1/4}}.$$

The Reynolds number is expressed by

$$\mathbf{Re} = \frac{\rho |v_x| Dh}{\mu}.$$

and the two-phase dynamic viscosity as

$$\mu = \mu_v x + \mu_L (1 - x).$$

Part III

Numerical Methods

Mixed finite volume discretization of 2D diffusion, advection and reaction models

In this chapter we describe the numerical techniques used for solving the air and panel physical models, presented in Chapters 2 and 3.

Whit this aim we will consider an advection, diffusion and reaction model problem to be solved on a rectangular domain and we will describe in detail a finite volume discretization method, properly designed for a stable, conservative and accurate approximation. The scheme will be interpreted as a dual mixed finite element method where suitable quadrature rules are adopted for the numerical computation of the flux mass matrix and the convective term.

A numerical validation of the accuracy and stability of the proposed scheme will be carried out on the solution of convection-diffusion test cases exhibiting steep boundary and internal layers.

5.1 The model problem

The air and panel wall physical models (2.6) and (3.3) can be expressed in the following general form

$$\begin{cases} \operatorname{div}(-\alpha \nabla \mathbf{u} + \beta \mathbf{u}) + \gamma \mathbf{u} = f & \text{in } \Omega, \\ + \text{boundary conditions} & \text{on } \Gamma, \end{cases} \quad (5.1)$$

on the rectangular domain Ω , with the appropriate boundary conditions on $\Gamma = \partial\Omega$. System (5.1) is an *advection, diffusion and reaction problem* where

$$\begin{cases} \operatorname{div}(-\alpha \nabla \mathbf{u}) & \rightarrow \text{conduction or diffusion term,} \\ \operatorname{div}(\beta \mathbf{u}) & \rightarrow \text{convection term,} \\ \gamma \mathbf{u} & \rightarrow \text{source or reaction term.} \end{cases}$$

u is the unknown variable, α is the diffusion coefficient, β is the given convection field and γ the absorption coefficient.

We assume that $f \in L^2(\Omega)$ and the following regularity constraints on the coefficients: $\alpha \in L^\infty(\Omega)$ and $\alpha(\mathbf{x}) \geq \alpha_0 > 0$, $\gamma \in L^2(\Omega)$ e $\gamma(\mathbf{x}) \geq 0$ in Ω , $\beta(\mathbf{x}) \in [L^\infty(\Omega)]^2$. Assuming coercivity of the differential problem

$$-\frac{1}{2}\operatorname{div}(\beta) + \gamma \geq \mu_0 > 0 \text{ in } \Omega,$$

the existence and uniqueness of the solution u of (5.1), in the distributional sense, immediately follow from the *Lax-Milgram* Lemma. For a proof see [Qua08, Chap. 5] and [Sal04].

The problem (5.1) can be written as a first order system

$$\begin{cases} \operatorname{div}(\mathbf{J}) + \gamma u & = f & \text{in } \Omega, \\ \mathbf{J} + \alpha \nabla u - \beta u & = \mathbf{0} & \text{in } \Omega, \\ \text{b.c.} & & \text{on } \Gamma, \end{cases} \quad (5.2)$$

where we have introduced the vector variable \mathbf{J} called flux.

5.2 Finite volume discretization

In this section we will describe a stabilized *cell-centered* finite volume discretization of problem (5.2), general form of the air and panel models.

We have decided to discretize the two dimensional domains involved in our problem using a cartesian rectangular mesh. This choice has pros and cons. An advantage of this choice is that working with rectangular cells we can avoid the use of mesh generator programs and the numerical solver can be implemented in ad hoc fashion. In addition, this choice allows an immediate interpretation of the discretized partial differential equations as balance equations in each rectangular cell. A disadvantage of this choice is that working with rectangular grids it is not straightforward to refine the grid only in some specifically targeted regions, so that, if a uniform refinement is adopted, the computational effort may increase significantly.

We introduce a decomposition \mathcal{T}_h of the domain Ω in N rectangles K , called *control volumes* or *cells*, such that $\cup \bar{K} = \bar{\Omega}$. Furthermore, we assume that the cells are pairwise disjoint.

Integrating the first equation of (5.2) in each cell K we obtain the system of equations

$$\int_{\partial K} \mathbf{J} \cdot \mathbf{n}_{\partial K} + \int_K \gamma u = \int_K f \quad \forall K \in \mathcal{T}_h, \quad (5.3)$$

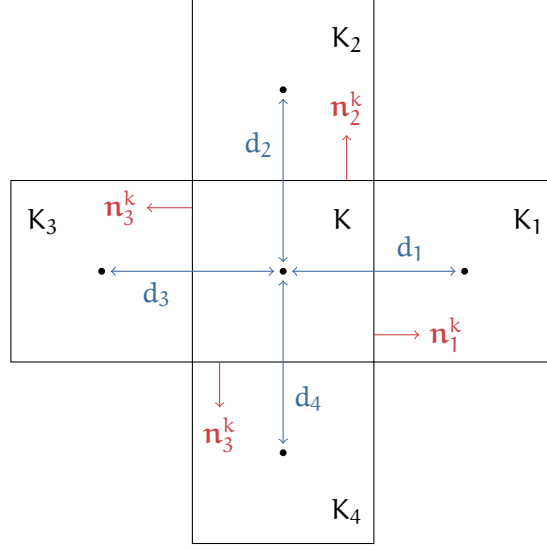


Figure 5.1: Computational stencil.

where $\mathbf{n}_{\partial K}$ is the outward unit vector on ∂K as shown in Figure 5.1. Denoting with e_q , for $q = 1, \dots, 4$, the four edges of K , equation (5.3) can be rewritten as

$$\sum_{q=1}^4 \int_{e_q} \mathbf{J} \cdot \mathbf{n}_q^k + \int_K \gamma u = \int_K f \quad \forall K \in \mathcal{T}_h,$$

where \mathbf{n}_q^k is the outward unit vector on the q -th edge of K .

Using a *cell-centered* finite volume method, the numerical solution u_h has only one degree of freedom for each cell, located in the center of gravity. We define \mathbb{Q}_k the space of polynomials that are of degree less than or equal to k with respect to each single variable x and y , then $u_h|_K \in \mathbb{Q}_0(K)$. We call u^K the constant value of the numerical solution in the cell K , i.e. $u_h|_K = u^K$.

The flux $\mathbf{J}|_{\partial K}$ can be approximated as the sum of four contributions, one for each edge of K , such that

$$\sum_{q=1}^4 j_q^K(u_h) |e_q| + \gamma_K u^K |K| = f_K |K|,$$

where $j_q^K(u_h)$ is the numerical flux through the q -th edge of K , γ_K and f_K are the values of the respective quantities evaluated in the center of gravity of K .

We will use the stabilized numerical flux

$$j_q^K(u_h) = -\frac{\alpha_q}{d_q} \left[\mathbb{B} \left(\frac{\beta_q d_q}{\alpha_q} \right) u^{K_q} - \mathbb{B} \left(-\frac{\beta_q d_q}{\alpha_q} \right) u^K \right] \quad q = 1, \dots, 4, \quad (5.4)$$

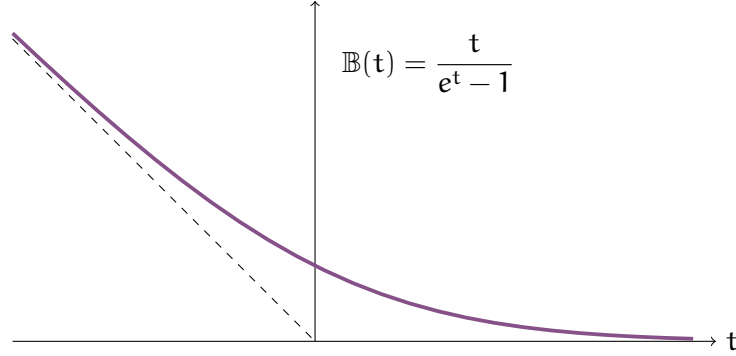


Figure 5.2: Trend of the inverse Bernoulli function.

derived from the *Scharfetter and Gummel* method (SG). K_q indicates the cell communicating with K across the edge e_q and d_q is the distance between the corresponding centers of gravity, as in Figure 5.1. The quantity α_q is the diffusion coefficient evaluated on e_q and β_q is defined as

$$\beta_q := \boldsymbol{\beta} \cdot \mathbf{n}_q^K,$$

i.e., it is the projection of the convective field on the outward unit vector \mathbf{n}_q^K on e_q . Since we decided to approximate α and $\boldsymbol{\beta}$ with piecewise-constant functions, to evaluate them on each edge we approximate α_q with the harmonic mean of α between K and K^q

$$\alpha_q \simeq \left(\frac{1}{d_q} \int_{\zeta}^{\zeta_q} \alpha^{-1} d\zeta \right)^{-1},$$

where ζ and ζ_q are the corresponding centers of gravity. Instead, we approximate β_q with the arithmetic mean between K and K^q

$$\beta_q \simeq \frac{\boldsymbol{\beta}^K + \boldsymbol{\beta}^{K_q}}{2} \cdot \mathbf{n}_q^K.$$

The *inverse Bernoulli function* is defined as

$$\begin{cases} \mathbb{B}(t) = \frac{t}{e^t - 1} & t \neq 0, \\ \mathbb{B}(0) = 1 & t = 0, \end{cases} \quad (5.5)$$

and it is depicted in Figure 5.2. Notice that $\mathbb{B}(t)$ is always positive, tends to zero for large positive values of t and is asymptotic to the line $f(t) = -t$ for large negative values of t .

In conclusion, the system of finite volume equations to solve is

$$\left[\sum_{q=1}^4 \frac{\alpha_q}{d_q} \mathbb{B} \left(-\frac{\beta_q d_q}{\alpha_q} \right) |\mathbf{e}_q| + \gamma_K |K| \right] u^K - \sum_{q=1}^4 \frac{\alpha_q}{d_q} \mathbb{B} \left(\frac{\beta_q d_q}{\alpha_q} \right) |\mathbf{e}_q| u^{K_q} = f_K |K|$$

$\forall K \in \mathcal{T}_h$. The corresponding algebraic problem is

$$\mathbf{M} \mathbf{u}_h = \mathbf{F}_h,$$

where $\mathbf{u}_h \in \mathbb{R}^N$ is the vector of unknown values of u_h , one for each K , and $\mathbf{F}_h \in \mathbb{R}^N$ is the vector of the right hand side term values. The matrix $\mathbf{M} \in \mathbb{R}^{N \times N}$ has the good property of being an M-matrix [QSS08, Chap. 1], effect of the stabilized method. In the discretization procedure of the air and panels model we do not need a high order discretization method, because of the contribution to the approximation even introduced by the empirical correlations. For this reason a piecewise-constant numerical solution u_h is a sensible choice, moreover the cell-centered finite volume approach favors the solver implementation.

5.3 Mixed finite volume discretization

In this section we will interpret the finite volume discretization just described, as a stabilized *Mixed Finite Volume* (MFV) method, extending the same approach used in [SS97] to the case of a cartesian rectangular mesh.

The mixed formulation of problem (5.1) is

$$\begin{cases} \mathbf{a} \mathbf{J} + \nabla \mathbf{u} - \mathbf{a} \beta \mathbf{u} = \mathbf{0} & \text{in } \Omega, \\ \operatorname{div}(\mathbf{J}) + \gamma \mathbf{u} = f & \text{in } \Omega, \\ \mathbf{u} = 0 & \text{on } \Gamma, \end{cases} \quad (5.6)$$

where we assume for simplicity homogeneous Dirichlet boundary conditions and $\mathbf{a} := \alpha^{-1}$ to be a constant quantity. In this formulation we have two different unknown variables, in addition to the scalar variable u there is a vector variable \mathbf{J} . Define the spaces

$$\begin{aligned} \mathbf{V} &\equiv H_{\operatorname{div}}(\Omega) = \{ \mathbf{v} : \mathbf{v} \in [L^2(\Omega)]^2, \operatorname{div}(\mathbf{v}) \in L^2(\Omega) \}, \\ \mathbf{Q} &\equiv L^2(\Omega), \end{aligned}$$

so that the dual mixed formulation of problem (5.6) reads:

find $\mathbf{J} \in \mathbf{V}$ and $u \in \mathbf{Q}$ such that

$$\begin{cases} \int_{\Omega} \mathbf{a} \mathbf{J} \cdot \boldsymbol{\tau} - \int_{\Omega} u \operatorname{div}(\boldsymbol{\tau}) - \int_{\Omega} \mathbf{a} u \beta \cdot \boldsymbol{\tau} = 0 & \forall \boldsymbol{\tau} \in \mathbf{V}, \\ \int_{\Omega} \Phi \operatorname{div}(\mathbf{J}) + \int_{\Omega} \gamma u \Phi = \int_{\Omega} f \Phi & \forall \Phi \in \mathbf{Q}. \end{cases} \quad (5.7)$$

The existence of the solution of (5.7) in the distributional sense is a consequence of the existence of a weak solution for (5.1). The coercivity, hence the uniqueness of the solution, is ensured assuming

$$\frac{\|\boldsymbol{\beta}\|_{L^\infty(\Omega)}}{\inf_{\Omega}(\gamma) \inf_{\Omega}(\alpha)} < 4.$$

In view of the numerical approximation of (5.7), we consider \mathcal{T}_h a regular decomposition of Ω into N_{el} rectangles K and we denote by θ_h the set of edges of \mathcal{T}_h and by N_{ed} the number of total edges of the mesh. Then, we denote by

$$\mathbb{P}_{k_1, k_2}(K) := \left\{ p(x, y) : p(x, y) = \sum_{l \leq k_1, m \leq k_2} b_{i,j} x^l y^m \right\}$$

the space of polynomials that are of degree less than or equal to k_1 with respect to x and less than or equal to k_2 with respect to y . From this we deduce that

$$\mathbb{Q}_k(K) = \mathbb{P}_{k,k}(K) \quad \forall k \geq 0.$$

Finally, we introduce the k -th order *Raviart-Thomas* (RT) mixed finite element space

$$\mathbb{RT}_{[k]}(K) := \mathbb{P}_{k+1,k}(K) \times \mathbb{P}_{k,k+1}(K) \quad k \geq 0.$$

Introducing the discrete subspaces of \mathbf{V} and \mathbf{Q}

$$\begin{aligned} \mathbf{V}_h &= \{ \mathbf{v}_h \in \mathbf{V} : \mathbf{v}_h|_K \in \mathbb{RT}_{[0]}(K) \forall K \in \mathcal{T}_h \}, \\ \mathbf{Q}_h &= \{ q_h \in \mathbf{Q} : q_h|_K \in \mathbb{Q}_0(K) \forall K \in \mathcal{T}_h \}, \end{aligned}$$

the discrete dual mixed problem reads:

find $u_h \in \mathbf{Q}_h$ and $\mathbf{J}_h \in \mathbf{V}_h$ such that

$$\begin{cases} \int_{\Omega} \mathbf{a} \mathbf{J}_h \cdot \boldsymbol{\tau}_h - \int_{\Omega} u_h \operatorname{div}(\boldsymbol{\tau}_h) - \int_{\Omega} \mathbf{a} u_h \boldsymbol{\beta} \cdot \boldsymbol{\tau}_h = 0 & \forall \boldsymbol{\tau}_h \in \mathbf{V}_h, \\ \int_{\Omega} \Phi_h \operatorname{div}(\mathbf{J}_h) + \int_{\Omega} \gamma u_h \Phi_h = \int_{\Omega} f \Phi_h & \forall \Phi_h \in \mathbf{Q}_h. \end{cases} \quad (5.8)$$

The pair of finite element spaces $\mathbb{Q}_0/\mathbb{RT}_{[0]}$ satisfies the *inf-sup* compatibility condition [QV08, Chap. 7].

The basis functions of the lowest-order RT finite element space are $\lambda_l \forall l \in \theta_h^{\text{in}}$, i.e. for each internal edge of \mathcal{T}_h . If we consider an internal vertical edge l , represented in Figure 5.3, the expression of λ_l is

$$\lambda_l = \begin{cases} \frac{x - x^+}{|K^+|} \mathbf{i} & \mathbf{x} \in K^+, \\ -\frac{x - x^-}{|K^-|} \mathbf{i} & \mathbf{x} \in K^-, \\ 0 & \text{elsewhere,} \end{cases}$$

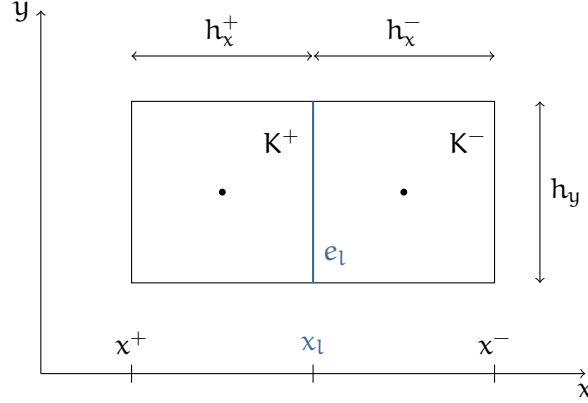


Figure 5.3: Two neighboring elements.

where \mathbf{i} is a unit vector in the direction x . This function is nonzero only in the two rectangles K^+ and K^- , which communicate through the edge l . With regard to the internal edges in the horizontal direction, there is an equivalent expression of λ_l as a function of y in the direction of \mathbf{j} , the unit vector in direction y . Instead, χ_m $\forall m \in \mathcal{T}_h^{\text{in}}$, i.e. for each internal volumes of \mathcal{T}_h , are the basis functions of \mathbb{Q}_0 , equal to one on the m -th cell and zero elsewhere.

Hence, we can express \mathbf{J}_h and u_h as

$$\begin{cases} \mathbf{J}_h(\mathbf{x}) = \sum_{l=1}^{\text{Ned}} \mathbf{j}_l \lambda_l(\mathbf{x}), \\ u_h = \sum_{m=1}^{\text{Nel}} u^m \chi_m(\mathbf{x}). \end{cases} \quad (5.9)$$

The second equation of system (5.8), choosing as test functions χ_k , becomes

$$\int_{\partial K} \mathbf{J}_h \cdot \mathbf{n}_{\partial K} + u^k \int_K \gamma dK = \int_K f dK \quad \forall K \in \mathcal{T}_h^{\text{in}},$$

and defining

$$\bar{\gamma}_k := \frac{1}{|K|} \int_K \gamma dK \quad \text{and} \quad \bar{f}_k := \frac{1}{|K|} \int_K f dK,$$

finally we get

$$\int_{\partial K} \mathbf{J}_h \cdot \mathbf{n}_{\partial K} + \bar{\gamma}_k |K| u^k = \bar{f}_k |K| \quad \forall K \in \mathcal{T}_h^{\text{in}}. \quad (5.10)$$

The equation (5.10) is a discrete conservation law. In this way, the original conservation equation (5.1) is expressed in integral form cell by cell. Indeed, the first term of (5.10) is the outgoing flux through ∂K , the second is the absorption contribution

in K and the right hand side is the source term contribution in K .

If we choose λ_l as test functions of the first equation of (5.8), for all the internal vertical edges we get

$$\int_{K^+ \cup K^-} \alpha J_{h_x} \lambda_{lx} - \int_{K^+ \cup K^-} u_h \partial_x \lambda_{lx} - \int_{K^+ \cup K^-} \alpha u_h \beta_x \lambda_{lx} = 0, \quad (5.11)$$

where the subscript $(\cdot)_x$ denotes the component in the x direction of the corresponding vector quantities. First of all, we notice that

$$\int_{K^+ \cup K^-} u_h \partial_x \lambda_{lx} = \left[u^{K^+} \int_{K^+} \partial_x \lambda_{lx} + u^{K^-} \int_{K^-} \partial_x \lambda_{lx} \right].$$

Then, we introduce two suitable quadrature rules in order to express the flux j_l on the internal edge l as a function of u^{K^+} and u^{K^-} . The first approximation is

$$\int_{K^+} u_h \lambda_{lx} + \int_{K^-} u_h \lambda_{lx} \simeq \bar{u}_l \left[\int_{K^+} \lambda_{lx} + \int_{K^-} \lambda_{lx} \right], \quad (5.12)$$

where \bar{u}_l is average value across the l -th edge, defined as

$$\bar{u}_l := \frac{u^{K^+} + u^{K^-}}{2}.$$

The second quadrature rule is

$$\begin{aligned} \int_{K^+ \cup K^-} J_{h_x} \lambda_{lx} &\simeq h_y \left\{ \left[(J_{h_x} \lambda_{lx})|_{x=x^+} + (J_{h_x} \lambda_{lx})|_{x=x_l} \right] \frac{h_x^+}{2} \right\} \\ &+ h_y \left\{ \left[(J_{h_x} \lambda_{lx})|_{x=x_l} + (J_{h_x} \lambda_{lx})|_{x=x^-} \right] \frac{h_x^-}{2} \right\}, \end{aligned} \quad (5.13)$$

which amounts to applying the trapezoidal quadrature rule in each volume considered. h_x^+ and h_x^- are the sizes in the x direction of K^+ and K^- respectively, while h_y is the size of both in direction y , see Figure 5.3.

Then, using the first expression of (5.9) and the two approximations (5.12) and (5.13), equation (5.11) becomes

$$\frac{j_l}{2} h_y \left(\frac{h_x^+}{h_y^2} + \frac{h_x^-}{h_y^2} \right) - \alpha (u^{K^+} - u^{K^-}) - \beta_x \bar{u}_l \left(\frac{h_x^+ + h_x^-}{2} \right) = 0,$$

hence the local flux contribution through each internal vertical edge is

$$j_l = \left[-\alpha \left(\frac{u^{K^-} - u^{K^+}}{H_x} \right) + \beta_x \left(\frac{u^{K^+} + u^{K^-}}{2} \right) \right] h_y,$$

where H_x is the distance between the centers of gravity of K^+ and K^- , defined as

$$H_x := \frac{h_x^+ + h_x^-}{2}.$$

The same steps can be retraced in the case where l is an internal horizontal edge, obtaining a similar result but in terms of the direction y .

In conclusion, the MFV approximation of problem (5.6) is

$$\begin{cases} \sum_{l \in \partial K} j_l + u^K \bar{\gamma}_k |K| = \bar{f}_k |K| & \forall K \in \mathcal{T}_h^{\text{in}}, \\ j_l = \left[-\alpha \left(\frac{u^{K_l} - u^K}{d_l} \right) + \beta_l \left(\frac{u^K + u^{K_l}}{2} \right) \right] |e_l| & l \in \partial K, \end{cases} \quad (5.14)$$

reformulated using the notation of Section 5.2 and Figure 5.1. The Dirichlet boundary conditions are imposed through the condition

$$u^{K_l} = 0 \quad \forall l \in \Gamma.$$

Notice that the numerical method described so far does not require the continuity of the solution J_h in \mathcal{T}_h , but only the continuity of its normal component on each edge of the mesh. Furthermore, the approximation error of this method has an optimal convergence order, equal to the maximum achievable with the regularity of the approximation functions used [BFM93].

The numerical flux in (5.14) is derived using a centered finite volume discretization, then the solution of (5.14) can exhibit an oscillatory behavior if the local *Péclet number*, defined as

$$\mathbb{P}e_l := \frac{|\boldsymbol{\beta} \cdot \mathbf{n}_l| d_l}{2\alpha} \quad \forall l \in \theta_h^{\text{in}},$$

is greater than one. In the case of dominating convection regime, one possible remedy to this instability is the reduction of the grid step d_l , increasing however the numerical complexity of simulations.

Alternatively, to end up with a stable and monotone numerical solution we can use the following appropriately modified version of (5.8)

$$\begin{cases} \int_{\Omega} \alpha J_h \cdot \boldsymbol{\lambda}_l - \int_{\Omega} u_h \operatorname{div}(\boldsymbol{\lambda}_l) - \int_{\Omega} \alpha u_h \boldsymbol{\beta} \cdot \boldsymbol{\lambda}_l - \sum_{l \in \theta_h^{\text{in}}} \int_l [[u_h]]_l \cdot \boldsymbol{\lambda}_l \rho_l ds = 0 \\ \int_{\Omega} \chi_m \operatorname{div}(J_h) + \int_{\Omega} \gamma u_h \chi_m = \int_{\Omega} f \chi_m & \forall l \in \theta_h^{\text{in}}, \forall m \in \mathcal{T}_h^{\text{in}}. \end{cases}$$

The added stabilization term is

$$- \int_l [[u_h]]_l \cdot \boldsymbol{\lambda}_l \rho_l ds \quad \forall l \in \theta_h^{\text{in}}$$

where $[[u_h]]_l$ is the jump of u_h across the edge l , defined as

$$[[u_h]]_l := u^K \mathbf{n}_l^K + u^{K_l} \mathbf{n}_l^{K_l},$$

and the stabilization function is $\rho_l = \rho_l(\mathbb{P}e_l)$, to be specified later.

Following the same approach used for (5.8), the MFV discretization of the modified problem is

$$\begin{cases} \sum_{l \in \partial K} j_l^{\text{stab}} + \mathbf{u}^K \bar{\gamma}_k |K| = \bar{f}_k |K| & \forall K \in \mathcal{T}_h^{\text{in}}, \\ j_l^{\text{stab}} = \left[-\alpha (1 + \rho_l) \left(\frac{\mathbf{u}^{K_l} - \mathbf{u}^K}{H_l} \right) + \boldsymbol{\beta} \cdot \mathbf{n}_l \left(\frac{\mathbf{u}^K + \mathbf{u}^{K_l}}{2} \right) \right] |\mathbf{e}_l| & l \in \partial K, \end{cases} \quad (5.15)$$

Two possible choices of the stabilization functions are:

- $\rho_l(\mathbb{P}e_l) = \mathbb{P}e_l$,
- $\rho_l(\mathbb{P}e_l) = \mathbb{P}e_l - 1 + \mathbb{B}(2\mathbb{P}e_l)$.

The first one corresponds to the *upwind* method, while the second corresponds to the SG method. In fact, replacing $\rho_l(\mathbb{P}e_l) = \mathbb{P}e_l - 1 + \mathbb{B}(2\mathbb{P}e_l)$ in (5.15), the numerical flux obtained coincides with the expression (5.4) introduced in the previous section. Both methods are *artificial viscosity methods*, in the next section we will make a comparison between them.

5.4 Comparison between upwind and SG methods

For simplicity we consider a one-dimensional restriction of the advection, diffusion and reaction problem (5.1). The domain Ω is the interval $(0,L)$, we define $N + 1$ nodes $x_0 = 0, \dots, x_N = L$, dividing the interval Ω into N segments.

The centered finite volume discretization of the first derivative term at node i is

$$u'_i \simeq \frac{u_{i+1} - u_{i-1}}{2\delta} \quad i = 1, \dots, N - 1,$$

where $\delta = L/N$ is the discretization step and u_i is the value of the unknown variable in the node i .

In this case the local Péclet number can be expressed as

$$\mathbb{P}e = \frac{|\boldsymbol{\beta}| \delta}{2\alpha}.$$

The stabilized problem, using the upwind or SG method, is an advection, diffusion and reaction problem of the form (5.2), with a modified flux

$$\tilde{\mathbf{J}}(\mathbf{u}) = -\alpha_h \nabla \mathbf{u} + \boldsymbol{\beta} \mathbf{u}.$$

The coefficient α_h is

$$\alpha_h = \alpha (1 + \phi(\mathbb{P}e)),$$

while the correction factor introduced $\alpha_h - \alpha$ is called *artificial viscosity*. Then the local Péclet number for the modified problem is

$$\mathbb{P}e^* = \frac{|\beta|\delta}{2\alpha_h} = \frac{\mathbb{P}e}{1 + \phi(\mathbb{P}e)} < 1 \quad \forall \delta > 0.$$

We can observe that $\phi(\mathbb{P}e)$ is the one-dimensional stabilizing function corresponding of $\rho_l(\mathbb{P}e)$.

The discretization matrix associated with the stabilized method is always an M-matrix irrespectively of δ , therefore the numerical solution is monotone without oscillations.

We can make a comparison between the properties of consistency, stability and convergence order of the three numerical methods introduced so far:

- centered difference method:
 1. consistent
 2. not stable if $\mathbb{P}e > 1$
 3. convergence order $O(\delta^2)$
- upwind method:
 1. weakly consistent, α is replaced by α_h
 2. stable, $\mathbb{P}e^* < 1 \forall \delta$
 3. convergence order $O(\delta)$
- SG method:
 1. weakly consistent, α is replaced by α_h
 2. stable, $\mathbb{P}e^* < 1 \forall \delta$
 3. convergence order $\begin{cases} \mathbb{P}e \rightarrow 0 & O(\delta^2) \\ \mathbb{P}e \rightarrow \infty & O(\delta) \end{cases}$

The convergence order in the above analysis is always referred to the $L^2(\Omega)$ norm of the projection error $\mathcal{P}_h u - u_h$, where $\mathcal{P}_h u$ is the L^2 -projection of the exact solution of (5.1) onto \mathbb{Q}_h . The SG method is called the upwind scheme with optimal viscosity, because it adds the minimum amount of artificial viscosity required to have a stable method. In a full dominating convection regime, i.e. $\mathbb{P}e \rightarrow \infty$

$$\mathbb{P}e - 1 + \mathbb{B}(2\mathbb{P}e) \simeq \mathbb{P}e,$$

so that, accordingly, the upwind method can be regarded as a limiting case of the SG method. For these reasons the SG scheme has been considered in the software implementation.

5.5 Validation of the discretization scheme

First of all we test the discretization errors of the upwind and SG methods, discussed in Section 5.4, on the following advection, diffusion and reaction model problem

$$\begin{cases} \operatorname{div}(-\alpha \nabla \mathbf{u} + \beta \mathbf{u}) + \gamma \mathbf{u} = \mathbf{f} & \text{in } \Omega \\ \mathbf{u} = \mathbf{g} & \text{on } \partial\Omega \end{cases} \quad (5.16)$$

where $\Omega = (0, 1) \times (0, 1)$. We impose the exact solution equal to

$$\mathbf{u}_{\text{ex}} = \cos x \sin y,$$

and the values of the parameter $\beta = [0, 1]^T$ and $\gamma = 1$, while the diffusion parameter is varying in

$$\alpha = \{1, 10^{-1}, 10^{-2}, 10^{-3}, 10^{-4}\},$$

in order to analyze both dominating convection or diffusion regimes. The right hand side \mathbf{f} is imposed such that \mathbf{u}_{ex} is solution of (5.16). We solve the problem (5.16) using both stabilization methods with computational cartesian grids of dimension varying from 4×4 to 64×64 .

In Figure 5.4 we plot the discrete maximum norm of the errors between the numerical and exact solution for each value of α and discretization step h .

For low values of the Péclet number $\mathbb{P}e$, corresponding for example to $\alpha = 1$, the SG method has a convergence order of $O(h^2)$, that decrease to $O(h)$ for dominating convection regimes, as for $\alpha = 10^{-4}$. On the other hand, the estimated convergence error of the upwind method is never greater than $O(h)$.

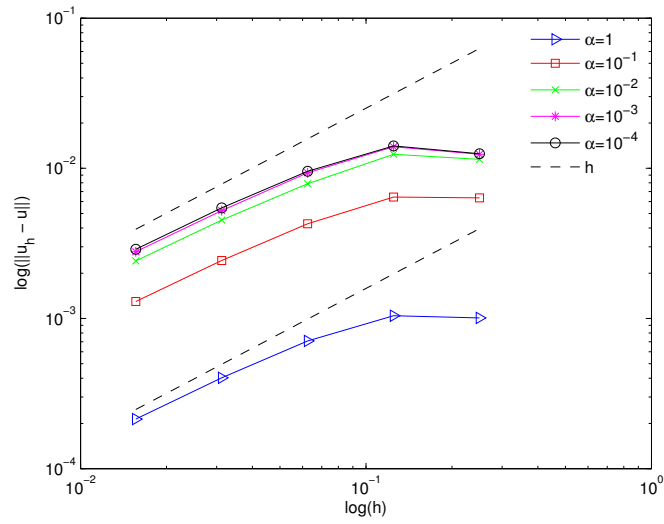
To validate the robustness of the SG method we use it to solve the numerical examples studied in [XZ99, p. 1442]. The first test problem is

$$\begin{cases} \operatorname{div}(-\alpha \nabla \mathbf{u} + [-y, x]^T \mathbf{u}) = 1 & (\mathbf{x}, \mathbf{y}) \in \Omega, \\ \mathbf{u} = 0 & (\mathbf{x}, \mathbf{y}) \in \partial\Omega, \end{cases} \quad (5.17)$$

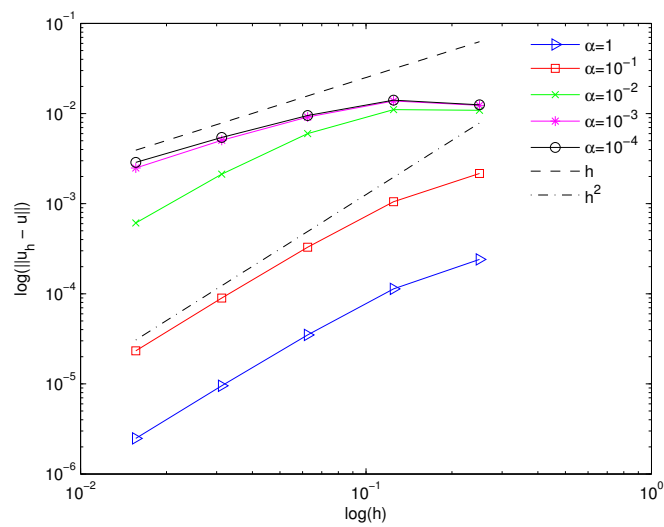
where the domain is $\Omega = (0, 1) \times (0, 1)$. Problem (5.17) allows to check how the numerical method is able to avoid the onset of spurious oscillations in the boundary layer region.

The second example studied is

$$\begin{cases} -\operatorname{div}(\alpha \nabla \mathbf{u} + \mathbf{u} \nabla \psi) = 0 & \mathbf{x} \in \Omega, \\ \mathbf{u} = \mathbf{l} & \mathbf{x} \in \Gamma_D, \\ \frac{\partial \mathbf{u}}{\partial \mathbf{n}} + \frac{\partial \psi}{\partial \mathbf{n}} \mathbf{u} = 0 & \mathbf{x} \in \Gamma_N, \end{cases} \quad (5.18)$$



(a) upwind



(b) SG

Figure 5.4: Test of convergence order for upwind and SG methods, problem (5.16). Logarithmic plot of the maximum norm of the errors between the numerical and exact solution, as a function of the discretization step h .

on the same domain Ω as in problem (5.17). The Dirichlet boundary conditions are imposed on Γ_D as follows

$$l = \begin{cases} 0 & \{x = 0, y \in [0, 0.25]\} \cup \{x \in [0, 0.25], y = 0\}, \\ 2.1 & \{x = 1, y \in [0.75, 1]\} \cup \{x \in [0.75, 1], y = 1\}, \end{cases}$$

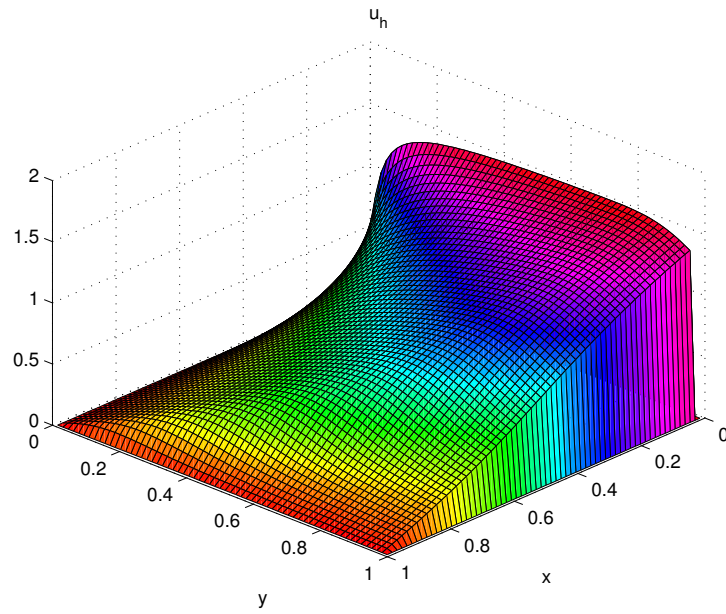
and the potential function ψ is defined as

$$\psi = \begin{cases} 0 & 0 \leq d + x < 0.55, \\ 2(d - 0.55) & 0.55 \leq d + x < 0.65, \\ 0.2 & 0.65 \leq d + x, \end{cases}$$

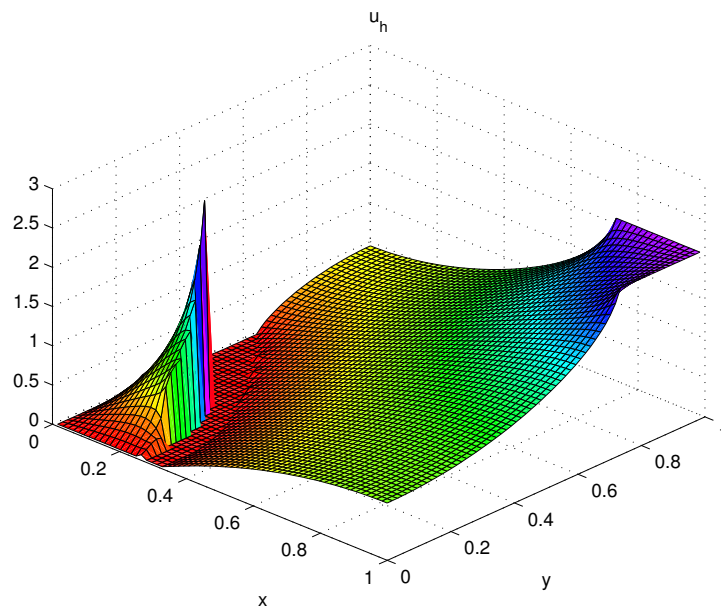
where $d = (x^2 + y^2)^{1/2}$. Through this example we want to test the ability of the SG method to deal with internal layers.

The numerical solutions obtained in these two examples are shown in Figure 5.5, in both cases $\alpha = 10^{-6}$ and $h = 2^{-6}$. For graphical purposes, the computed values of u_h have been interpolated through a nodally continuous function.

Results are in complete agreement with physical intuition and show the robustness of the scheme with respect to dominating convection problems.



(a) problem (5.17)



(b) problem (5.18)

Figure 5.5: Surface plot of the numerical solutions using the SG method, problems (5.17) and (5.18).

Galerkin and Petrov-Galerkin discretization of 1D fluid equation

In this chapter we will focus on the description of the numerical techniques used for the discretization of the two-phase fluid equations.

The models, derived in Chapter 4, are only in the case of horizontal or vertical trunk of pipes, while the geometry of the channel crossing the condenser panel consists of a set of vertical and horizontal segments, curves at right angles and T-junctions respectively. The last type of elements is present only if the channel splits in two or more branches.

The idea is to consider, also for the whole channel, a one-dimensional approximation of the physical problem along the curvilinear coordinate. Using this interpretation, the vertical and horizontal models derived in Chapter 4 are the two basis cases.

For the incompressible flow model we will analyze the discrete problem considering both cases of channel with splits in branches or without. Instead for the compressible fluid case we only analyze the case of channel without splitting.

6.1 Single-phase incompressible fluid

We consider now a channel with an arbitrary geometry Ω , constant cross section and crossed by a single-phase incompressible fluid. We remark that the density is assumed constant under the assumption of incompressibility.

As a first approximation, we neglect the gravity effect in the vertical trunks of channel, in order to have the same physical problem in each segment. However, we include the possibility of channel splitting, hence the variable m is no more globally constant, but only locally in each segment.

To derive the mathematical model, we start from (4.4) and we get \dot{m} from the momentum equation as

$$\dot{m} = -\frac{1}{R(\Sigma, \mu, \rho)} \partial_s p.$$

Substituting this relation in the mass balance equation, we obtain a *Laplace problem* for p

$$\partial_s \dot{m} = \partial_s \left(-\frac{1}{R(\Sigma, \mu, \rho)} \partial_s p \right) = 0.$$

Under the assumptions of constant cross section, the hydraulic resistance $R(\Sigma, \mu, \rho)$ is constant in each trunk, so that the mathematical model can be written as

$$\begin{cases} -\frac{1}{R} \partial_s^2 p = 0 \\ \partial_s (-\alpha \partial_s T + \beta T + \dot{m} p) + \gamma(T - T_w) = 0 \end{cases} \quad \text{in } \Omega, \quad (6.1)$$

where s is the curvilinear coordinate.

If we consider for a moment to reintegrate the gravity effect in the trunks where the coordinate s is equal to the vertical one, the first equation of (6.1) can be replaced by a more general *Poisson problem* for the pressure

$$-\frac{1}{R(\Sigma, \mu, \rho)} \partial_s^2 p = f,$$

where the right hand side is due to the gravity force.

Problem (6.1) is a system of two advection, diffusion and reaction equations, the first one being a particular case of only diffusion. For this reason we can describe in detail the discretization of only the energy balance problem

$$(-\alpha T' + \beta T + \dot{m} p)' + \gamma T = \gamma T_w \quad \text{in } \Omega, \quad (6.2)$$

where derivatives are taken with respect to the curvilinear coordinate s .

We define a segmentation of the channel Ω in a set of horizontal and vertical trunks, which we will call elements. For each element there are two boundary points which we call nodes; if there is a division in branches the splitting point corresponds to a node of the discretization. We denote with $s_0 = \Gamma_{\text{in}} \leq s_1 \leq \dots \leq s_N = \Gamma_{\text{out}}$ the points of the segmentation, where Γ_{in} and Γ_{out} are the inlet and outlet nodes respectively. Even if we have $N + 1$ nodes the number of elements N_{el} can be larger than N , because of the splittings.

The weak formulation and the respective Galerkin formulation of problem (6.2) are a particular case of the general advection, diffusion and reaction problem, already analyzed in Chapter 5.

We will consider piecewise-linear approximations p_h and T_h of the variables p and

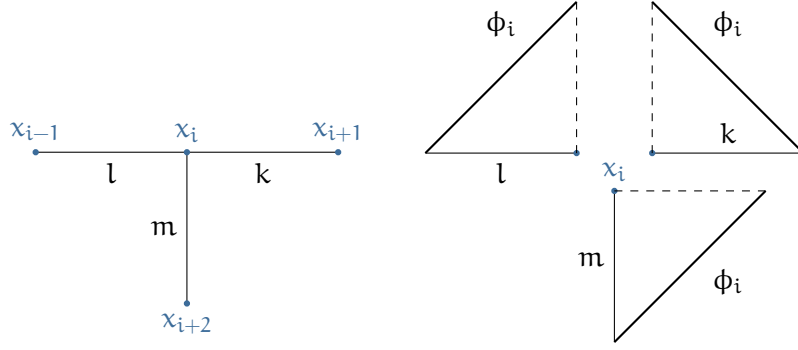


Figure 6.1: An example of piecewise-linear base function for a splitting node case.

T respectively, i.e. in each element of the discretization $p_h \in \mathbb{P}_1$ and $T_h \in \mathbb{P}_1$, where we denote with \mathbb{P}_k the space of polynomials that are of degree less than or equal to k with respect to the variable s .

The piecewise-linear continuous basis functions ϕ_i , for $i = 0, \dots, N$, are non zero only in the two or more elements communicating through the node x_i . To clarify the idea, a representation of ϕ_i is shown in Figure 6.1, where there are three segments of channel communicating through one single point.

If we use ϕ_i as test functions in the Galerkin method applied to (6.2), we get

$$\int_{\Omega} \alpha T_h' \phi_i' - \int_{\Omega} (\beta T_h + m p_h) \phi_i' + \int_{\Omega} \gamma (T_h - T_w) \phi_i = 0 \quad i = 1, \dots, N-1. \quad (6.3)$$

Referring to Figure 6.1, we can analyze each single term in (6.3). The diffusion term is equal to

$$\int_{\Omega} \alpha T_h' \phi_i' = \frac{1}{L_l} \int_{x_{i-1}}^{x_i} \alpha T_h' - \frac{1}{L_k} \int_{x_i}^{x_{i+1}} \alpha T_h' - \frac{1}{L_m} \int_{x_i}^{x_{i+2}} \alpha T_h',$$

where L_l , L_k and L_m are the size of the respective elements. Assuming the coefficients α , β , γ and m piecewise-constant functions and noting that

$$T_h(s) = \sum_{i=0}^{i=N} T_i \phi_i(s),$$

we get

$$\int_{\Omega} \alpha T_h' \phi_i' = \alpha_l \frac{T_i - T_{i-1}}{L_l} - \alpha_k \frac{T_{i+1} - T_i}{L_k} - \alpha_m \frac{T_{i+2} - T_i}{L_m}.$$

The same can be done for the convective contributions:

$$- \int_{\Omega} \beta T_h \phi_i' = -\beta_l \frac{T_i + T_{i-1}}{2} + \beta_k \frac{T_i + T_{i+1}}{2} + \beta_m \frac{T_i + T_{i+2}}{2},$$

and an identical one received for the imp_h contribution. In conclusion, if we use the trapezoidal quadrature rule for the contribution due to the reaction and source terms, we get

$$\int_{\Omega} \gamma(T_h - T_w)\phi_i \simeq \gamma_l \frac{L_l}{2}(T_i - T_{wi}) + \gamma_k \frac{L_l}{2}(T_i - T_{wi}) + \gamma_l \frac{L_m}{2}(T_i - T_{wi}).$$

Then we can write the discrete balance equation of fluxes at node i as:

$$j_{i,l} + j_{i,k} + j_{i,m} = 0,$$

where $j_{i,l}$ is the contribution at the node i due to the element l , expressed as

$$j_{i,l}(T_h, p_h) = \alpha_l \frac{T_i - T_{i-1}}{L_l} - \beta_l \frac{T_i + T_{i-1}}{2} - \dot{m}_l \frac{p_i + p_{i-1}}{2} + \gamma_l \frac{L_l}{2}(T_i - T_{wi}),$$

and where the contributions due to the elements k and m have a similar expression. Using the same approach for each node, we end up with the following system of algebraic equations

$$\sum_{l=1}^{\text{Nel}} j_{i,l}(T_h, p_h) = 0 \quad i = 1, \dots, N. \quad (6.4)$$

To derive a general expression of the contribution $j_{(i,l)}$, we define the connectivity matrix $C \in \mathbb{R}^{2 \times \text{Nel}}$: the column index corresponds to an element of the mesh and each column contains the two indexes of the nodes belonging to the corresponding element. For example, if we refer to Figure 6.1

$$C(\cdot, l) = \begin{bmatrix} i-1 \\ i \end{bmatrix}, C(\cdot, k) = \begin{bmatrix} i \\ i+1 \end{bmatrix} \text{ and } C(\cdot, m) = \begin{bmatrix} i \\ i+2 \end{bmatrix}. \quad (6.5)$$

Using this convention, for each element $k = 1, \dots, \text{Nel}$ the local contributions are

$$\left\{ \begin{array}{l} j_{C(1,k),k} = \left(-\frac{\alpha_k}{L_k} + \frac{\beta_k}{2} \right) T_{C(2,k)} + \left(\frac{\alpha_k}{L_k} + \frac{\beta_k}{2} + \gamma_k \frac{L_k}{2} \right) T_{C(1,k)} \\ \quad + \frac{\dot{m}_k}{2} p_{C(2,k)} + \frac{\dot{m}_k}{2} p_{C(1,k)} - \gamma_j \frac{L_j}{2} T_{wC(1,k)}, \\ j_{C(2,k),k} = \left(\frac{\alpha_k}{L_k} - \frac{\beta_k}{2} + \gamma_k \frac{L_k}{2} \right) T_{C(2,k)} + \left(-\frac{\alpha_k}{L_k} - \frac{\beta_k}{2} \right) T_{C(1,k)} \\ \quad - \frac{\dot{m}_k}{2} p_{C(2,k)} - \frac{\dot{m}_k}{2} p_{C(1,k)} - \gamma_j \frac{L_j}{2} T_{wC(1,k)}. \end{array} \right.$$

The derived discretization can exhibit oscillatory numerical solutions, so that to remedy this instability problem we adopt the upwind stabilization method, already described in Chapter 5 for the case of the air and panel discretization. The

corresponding stabilized contribution of each element $k = 1, \dots, Nel$ are

$$\left\{ \begin{array}{l} j_{C(1,k),k} = \left(-\frac{\alpha_k}{L_k} + \beta_k^- \right) T_{C(2,k)} + \left(\frac{\alpha_k}{L_k} + \beta_k^+ + \gamma_k \frac{L_k}{2} \right) T_{C(1,k)} \\ \quad + \dot{m}_k^- p_{C(2,k)} + \dot{m}_k^+ p_{C(1,k)} - \gamma_j \frac{L_j}{2} T_{wC(1,k)}, \\ j_{C(2,k),k} = \left(\frac{\alpha_k}{L_k} - \beta_k^- + \gamma_k \frac{L_k}{2} \right) T_{C(2,k)} + \left(-\frac{\alpha_k}{L_k} - \beta_k^+ \right) T_{C(1,k)} \\ \quad - \dot{m}_k^- p_{C(2,k)} - \dot{m}_k^+ p_{C(1,k)} - \gamma_j \frac{L_j}{2} T_{wC(1,k)}, \end{array} \right. \quad (6.6)$$

where we define

$$\left\{ \begin{array}{l} \dot{m}_k^+ = \frac{\dot{m}_k + |\dot{m}_k|}{2} \\ \dot{m}_k^- = \frac{\dot{m}_k - |\dot{m}_k|}{2} \end{array} \right. \quad (6.7)$$

and a similar expression for β_k .

Applying the same approach to the Laplace problem in the variable p_h we get

$$\sum_{l=1}^{Nel} q_{i,l}(p_h) = 0 \quad i = 1, \dots, N, \quad (6.8)$$

where the contributions of each element are

$$\left\{ \begin{array}{l} q_{C(1,k),k} = -\frac{p_{C(2,k)} - p_{C(1,k)}}{R_k L_k}, \\ q_{C(2,k),k} = \frac{p_{C(2,k)} - p_{C(1,k)}}{R_k L_k}, \end{array} \right. \quad (6.9)$$

being R_k the constant value of R in the k -th element.

Till now we have neglected the gravity effect in the vertical trunks of channel; if we now include this effect in the elements k that are vertical, the corresponding local contributions are

$$\left\{ \begin{array}{l} j_{C(1,k),k}^v = j_{C(1,k),k}^h + \rho g (\dot{m}_k^- y_{C(2,k)} + \dot{m}_k^+ y_{C(1,k)}), \\ j_{C(2,k),k}^v = j_{C(2,k),k}^h - \rho g (\dot{m}_k^- y_{C(2,k)} + \dot{m}_k^+ y_{C(1,k)}), \end{array} \right.$$

and

$$\left\{ \begin{array}{l} q_{C(1,k),k}^v = q_{C(1,k),k}^h - \rho g \frac{y_{C(2,k)} - y_{C(1,k)}}{R_k L_k}, \\ q_{C(2,k),k}^v = q_{C(1,k),k}^h + \rho g \frac{y_{C(2,k)} - y_{C(1,k)}}{R_k L_k}, \end{array} \right.$$

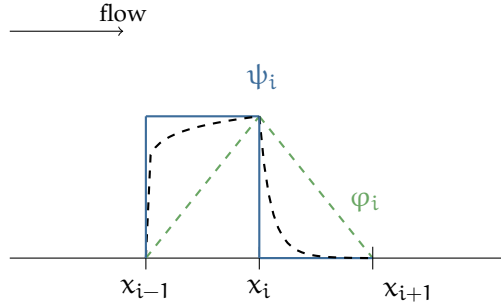


Figure 6.2: Upwind Petrov-Galerkin linear basis functions.

where g is the acceleration of gravity in the vertical direction and y are the coordinates of the nodes in the vertical direction. The superscript v or h denotes the contributions in the horizontal or vertical cases, the expressions of j^h and q^h are (6.6) and (6.9).

We notice that, in the way we have expressed the contributions j^v and q^v , they are also valid in the horizontal elements k where $y_{C(2,k)} - y_{C(1,k)} = 0$.

We will discuss later, in Chapter 7, how to impose the corresponding boundary conditions to the obtained algebraic systems.

Remark The upwind stabilization method can be interpreted as the following *Petrov-Galerkin Method*

$$\text{find } u_h \in \mathbf{V}_h : \quad a(u_h, v_h) = F_h(v_h) \quad \forall v_h \in \mathbf{W}_h, \quad (6.10)$$

where the space of the test functions \mathbf{W}_h does not coincide with the space \mathbf{V}_h where we search the solution. For a detailed analysis of this interpretation see [BH82] and [QV08]. The basis function of \mathbf{W}_h can be written as

$$\psi_i = \phi_i + \lambda_i \quad \forall i,$$

where ϕ_i are the basis functions of \mathbf{V}_h and λ_i are suitable bubble functions.

In Figure 6.2 we compare the upwind Petrov-Galerkin basis function ψ_i to the linear finite element basis function ϕ_i of \mathbf{V}_h .

6.2 Two-phase compressible fluid

In this case we have to describe separately the discretization of the differential equations (4.9) and of the algebraic constraints due to the two-phase liquid-vapor

constitutive relations (4.11).

Problem (4.9) is a system of one-dimensional parabolic differential equations, as for the incompressible flow. As previously mentioned we will focus on the case of no splitting channel, hence the variable G_s is constant in all the channel and is equal to the input variable, where s is the curvilinear coordinate. To ease the notation we remove the subscript s , but all the quantities and derivatives are to be considered in the curvilinear direction.

We first deal with the discretization of the system (4.9) solving

$$\begin{cases} G v' + p' - f = 0 \\ G h' + \eta(T - T_w) = 0 \end{cases} \quad \text{in } \Omega, \quad (6.11)$$

where $\eta = |\partial\Sigma|/h_{wc}$, and using the upwind Petrov-Galerkin method. The discrete solution of v_h , p_h , T_h and h_h are assumed to be piecewise-linear in Ω , while the test functions are ψ_i shown in Figure 6.2.

Using the same technique of discretization applied in Section 6.1 for the energy equation (6.2) to each equation of system (6.11), we get the following discrete algebraic system

$$\begin{cases} \sum_{l=1}^{Nel} r_{i,l}(v_h, p_h, T_h) = 0 & i = 1, \dots, N, \\ \sum_{l=1}^{Nel} s_{i,l}(h_h, T_h) = 0 & i = 1, \dots, N, \end{cases} \quad (6.12)$$

where

$$\begin{cases} r_{C(1,k),k} = (v_{C(2,k)} - v_{C(1,k)}) G^- + (p_{C(2,k)} - p_{C(1,k)}) \frac{G^-}{G} \\ \quad - \frac{L_k}{2} f(G, x_{C(1,k)}, T_{C(1,k)}) \frac{G^-}{G}, \\ r_{C(2,k),k} = (v_{C(2,k)} - v_{C(1,k)}) G^+ + (p_{C(2,k)} - p_{C(1,k)}) \frac{G^+}{G} \\ \quad - \frac{L_k}{2} f(G, x_{C(2,k)}, T_{C(2,k)}) \frac{G^+}{G}, \end{cases}$$

and

$$\begin{cases} s_{C(1,k),k} = (h_{C(2,k)} - h_{C(1,k)}) G^- - \eta_k \frac{L_k}{2} (T_{C(1,k)} - T_{wC(1,k)}) \frac{G^-}{G}, \\ s_{C(2,k),k} = (h_{C(2,k)} - h_{C(1,k)}) G^+ - \eta_k \frac{L_k}{2} (T_{C(2,k)} - T_{wC(2,k)}) \frac{G^-}{G}. \end{cases}$$

G^+ and G^- are defined as (6.7) and the quantity η_k denotes the parameter η evaluated constant in each element, as the arithmetic mean between the values of η_k in

the two nodes.

The two-phase constitutive relations (4.11) can be approximated $\forall i$ as

$$\begin{cases} G &= v_i \left(\frac{\rho_V(T_i)\rho_L(T_i)}{\rho_V(T_i)(1-x_i) + \rho_L(T_i)x_i} \right), \\ h_i &= h_L(T_i)(1-x_i) + h_V(T_i)x_i, \\ p_i &= p(T_i), \end{cases} \quad (6.13)$$

where all the single-phase quantities ρ_l , ρ_v , h_L and h_V and p functions are evaluated using the fluid temperature at the node.

Computational algorithms

The aim of this chapter is the description of the main implementation features of the numerical solver developed in this thesis.

As mentioned previously, all the computer routines were implemented ad hoc using the MATLAB environment and programming language. In addition, we have exploited the Optimization Toolbox of MATLAB for the iterative solution of the nonlinear algebraic systems, arising from the three differential problems discussed in the previous chapters. The nonlinear dependence is mostly due to the physical properties of the air, aluminum wall and refrigerant fluid.

In practice, we have introduced this nonlinearity in the implemented routines using the program REFPROP, which uses the most accurate equations available in the literature to determine the thermodynamic and transport properties of fluids or mixtures. This program is authored, maintained and distributed by the National Institute of Standards and Technology (NIST).

7.1 Algebraic systems

We describe the nonlinear algebraic system associated with each subsystem considered, focusing on the properties of the matrices.

7.1.1 Air

The algebraic equation for the air problem (2.6) are

$$\mathcal{A}_a \mathbf{T}_a + \mathcal{R}_{aw} (\mathbf{T}_a - \mathbf{T}_w) = 0, \quad (7.1)$$

where $\mathbf{T}_a, \mathbf{T}_w \in \mathbb{R}^{N_{el} \times 1}$ are vectors containing the values of the air temperature and wall temperature respectively, evaluated at the center of gravity of each control

volume. The total number of control volumes is N_{el} . The matrix $\mathcal{A}_a \in \mathbb{R}^{N_{el} \times N_{el}}$ is the discrete analogue of the divergence term. The matrix $\mathcal{R}_{aw} \in \mathbb{R}^{N_{el} \times N_{el}}$ is a diagonal matrix, such that

$$\mathcal{R}_{aw}[i, j] = \begin{cases} \tilde{h}_{aw}(\mathbf{T}_a[i]) & \text{if } i = j, \\ 0 & \text{if } i \neq j. \end{cases} \quad (7.2)$$

The problem (7.1) is a nonlinear algebraic system, the nonlinearity coming from the fact that all the elements of the matrices \mathcal{A}_a and \mathcal{R}_{aw} depend on the values of the unknown variables. In fact, $\mathcal{R}_{aw} = \mathcal{R}_{aw}(\mathbf{T}_a)$ through the empirical correlation of the heat transfer coefficient between air and panel h_{aw} and $\mathcal{A}_a = \mathcal{A}_a(\mathbf{T}_a)$ through the air physical properties k , c_p and ν .

To solve this nonlinear system we have used the *Newton method* described in [QSS08, p. 222]. In order to optimize the computational effort of the procedure, we adopt the following first-order approximation of the Jacobian matrix

$$\mathcal{J}_a = \partial_{\mathbf{T}_a} [\mathcal{A}_a \mathbf{T}_a + \mathcal{R}_{aw} (\mathbf{T}_a - \mathbf{T}_w)] \simeq \mathcal{A}_a + \mathcal{R}_{aw}.$$

Without this approximation it would be necessary to use numerical techniques to approximate the Jacobian, slowing significantly the simulations. Using this rough approximation of the Jacobian matrix increases in general the number of iterations necessary to reach convergence; despite this, the gain in the computational effort is significant.

For example, solving only the air domain problem imposing the wall temperature constant T_w and a cartesian rectangular mesh of dimension 20×20 , we can compare the two results. Using the Jacobian matrix \mathcal{J}_a , fixed a tolerance of 10^{-12} , the iterative method reaches convergence in ten iterations for a total of 0.91s, instead approximating the Jacobian matrix using finite difference methods the number of iterations necessary to reach convergence is only five but the computational time is 33.38s. Therefore we deduce that even if the number of iterations is twice, the computational profit is almost 97%.

We notice that, actually, the physical and thermodynamical properties of the air are functions of air temperature and pressure. We neglect the dependence on the pressure assuming $p = 1 \text{ atm}$, the atmosphere pressure. Accordingly, the air pressure drop is post-calculated through the expression (2.9) and the friction factor empirical correlations.

Nu Correlations

Related to the implementation of the air model correlations, we have found some difficulty for the Bhatti and Shah entrance region correction of the Nusselt number

described in Section 2.2.1.

The definition (2.8) is written in terms of the averaged corrected Nusselt number $\overline{\mathbf{Nu}}$, while we are interested to calculate the corresponding local one \mathbf{Nu} .

If we consider for simplicity a duct of length L , in this case the definition of the average Nusselt number is

$$\overline{\mathbf{Nu}}_L = \frac{1}{L} \int_0^L \mathbf{Nu} \, dx.$$

Dividing the interval $(0, L)$ in n points such as $x_0 = 0 < x_1 \leq \dots \leq x_n = L$, then we can approximate the local Nusselt number in the node x_i as

$$\begin{aligned} \mathbf{Nu}_i &\simeq \frac{\overline{\mathbf{Nu}}_i x_i - \overline{\mathbf{Nu}}_{i-1} x_{i-1}}{x_i - x_{i-1}} = \frac{\int_0^{x_i} \mathbf{Nu} \, dx - \int_0^{x_{i-1}} \mathbf{Nu} \, dx}{x_i - x_{i-1}} = \\ &= \frac{1}{x_i - x_{i-1}} \int_{x_{i-1}}^{x_i} \mathbf{Nu} \, dx, \end{aligned}$$

where

$$\overline{\mathbf{Nu}}_i = \frac{1}{x_i} \int_0^{x_i} \mathbf{Nu} \, dx.$$

In other words, we approximate the local Nusselt number at the distance x_i from the entrance of the tube with the average Nusselt number calculated at the distance $x_i - x_{i-1}$, i.e. the size of the i -th element of discretization.

Another problem during the implementation of this entrance correction is the limitation $\frac{l}{D_h} > 3$, where l is the distance from the entrance of the pipe. This limitation is due to the fact that for $l \rightarrow 0$ accordingly $\overline{\mathbf{Nu}} \rightarrow \infty$.

We define as inlet cells all the cells of the domain where the maximum distance from the entrance is lower than three times the hydraulic diameter. For the inlet cells we assume that \mathbf{Nu} is equal to the value in the first next cells not belonging to the inlet. Through this approximation we limit the over-prediction and the gap of the heat transfer coefficient between the control volumes.

7.1.2 Panel

The nonlinear algebraic equations for the two-dimensional aluminum panel problem (3.3) are

$$\mathcal{A}_w \mathbf{T}_w + \mathcal{R}_{aw} (\mathbf{T}_w - \mathbf{T}_a) + \mathcal{R}_{wc} (\mathbf{T}_w - \mathbf{T}_c) = 0 \quad (7.3)$$

where \mathcal{A}_w , \mathcal{R}_{wa} , and $\mathcal{R}_{wc} \in \mathbf{R}^{Nel \times Nel}$ and $\mathbf{T}_c \in \mathbf{R}^{Nel \times 1}$ is the vector of two-phase fluid temperature in the center of gravity of each element, hence equal to zero in the panel cells not crossed by the channel. The diagonal matrix \mathcal{R}_{wc} has the same structure as \mathcal{R}_{aw} in (7.2), but in this case the rows corresponding to the panel cells not crossed by the channel are completely null.

Also the algebraic system (7.3) is non linear, the corresponding approximate Jacobian for the Newton method is

$$\mathcal{J}_w = \mathcal{A}_w + \mathcal{R}_{aw} + \mathcal{R}_{wc}.$$

The only physical property of the aluminum involved in the model is thermal conductivity, in this case its value is calculated interpolating the Table A.1 [IDW02, p. 905] as a function of temperature T_w .

Noting the similarity in the structures of the air and panel algebraic systems, we have decided to solve the coupled problem

$$\begin{bmatrix} \mathcal{A}_a + \mathcal{R}_{aw} & -\mathcal{R}_{aw} \\ -\mathcal{R}_{aw} & \mathcal{A}_w + \mathcal{R}_{aw} + \mathcal{R}_{wc} \end{bmatrix} \cdot \begin{bmatrix} T_a \\ T_w \end{bmatrix} = \begin{bmatrix} \mathbf{0} \\ \mathcal{R}_{wc} T_c \end{bmatrix}, \quad (7.4)$$

where the two-phase refrigerant temperature T_c is assumed to be known. Using the same approach, the approximate Jacobian matrix is

$$J_{aw} = \begin{bmatrix} \mathcal{A}_a + \mathcal{R}_{aw} & -\mathcal{R}_{aw} \\ -\mathcal{R}_{aw} & \mathcal{A}_w + \mathcal{R}_{aw} + \mathcal{R}_{wc} \end{bmatrix}.$$

In this case, if we rewrite the system (7.4) as

$$\mathcal{F}(\mathbf{Z}) = \mathbf{0} \quad \text{where} \quad \mathbf{Z} = \begin{bmatrix} T_a \\ T_w \end{bmatrix},$$

given an initial solution \mathbf{Z}^0 , at each iteration k the Newton method, with approximated Jacobian matrix, amounts to solving the linear system

$$J_{aw}(\mathbf{Z}^k) \delta \mathbf{Z}^k = -\mathcal{F}(\mathbf{Z}^k),$$

from which we update the solution vector through

$$\mathbf{Z}^{k+1} = \mathbf{Z}^k + \delta \mathbf{Z}^k.$$

7.1.3 Channel

As explained in detail in Chapter 4, each ordinary differential equations and each two-phase constitutive relations, in both cases of compressible and incompressible fluid, have a corresponding algebraic system of the form

$$\mathcal{N}(\mathbf{u}) = \mathcal{M}(\mathbf{u}) \mathbf{u} = \mathbf{0}, \quad (7.5)$$

where $\mathbf{U} \in \mathbb{R}^N$ is the vector of the corresponding unknown variables. \mathbf{N} are the total degree of freedom of the discrete solution considered. $\mathcal{N} \in \mathbb{R}^N$ and $\mathcal{M} \in \mathbb{R}^{N \times N}$ are implicitly expressed as function of \mathbf{U} .

To solve this nonlinear implicit system, the nonlinearity being always introduced by the definition of the single and two-phase physical and thermodynamical properties, we apply the Newton method. At the k -th iteration it solves the linear system

$$\mathcal{J}(\mathbf{u}^k) \delta \mathbf{u}^k = -\mathbf{N}(\mathbf{u}^k),$$

where $\mathbf{u}^{k+1} = \mathbf{u}^k + \delta \mathbf{u}^k$ and the Jacobian matrix is defined as

$$\mathcal{J}[h, l] = \frac{\partial \mathbf{N}[h]}{\partial \mathbf{U}[l]} \quad h, l = 1, \dots, N.$$

If we consider the algebraic system in form (7.5) corresponding to any discrete constitutive relations of (6.13), \mathcal{M} and consequently the Jacobian matrix have a diagonal pattern.

Instead, in the case of discretized ordinary differential equation, as (6.4), (6.8) and (6.12), the structure of the corresponding matrix \mathcal{M} is less immediate to obtain. In this case, to assemble the matrices we have used the approach of the *Nodal Analysis* [HRB75], primarily used in problems concerning electrical circuits. When the equations are expressed as discrete balance of the contributions sum in each node, element by element we can calculate the local contribution to \mathcal{M} and then plug it in the global matrix. This approach can be used both for \mathcal{M} and \mathcal{J} . To better explain this procedure, we consider the first system of equations of (6.12):

$$\sum_{l=1}^{Nel} r_{i,l}(v_h, p_h, T_h) = 0 \quad i = 1, \dots, N,$$

where Nel is the total number of element and N is the total number of nodes. Recalling the definition of connectivity matrix (6.5), the local contribution of the element l to the matrix \mathcal{M} is

$$\mathbf{M}_l = \begin{bmatrix} r_{C(1,l),l} \\ r_{C(2,l),l} \end{bmatrix}.$$

Therefore, the local contribution can be plugged in the global matrix as

$$\mathcal{M}[C(g, l), l] = \mathbf{M}_l[g, 1] \quad g = 1, 2.$$

Also for the Jacobian matrix, at the local level we compute the derivative of \mathbf{M}_l with respect to all the unknown variables at each node of the element. For example

$$\frac{\partial \mathbf{M}_l}{\partial \mathbf{v}_h} = \begin{bmatrix} \frac{\partial r_{C(1,l),l}}{\partial v_{C(1,l)}} & \frac{\partial r_{C(1,l),l}}{\partial v_{C(2,l)}} \\ \frac{\partial r_{C(2,l),l}}{\partial v_{C(1,l)}} & \frac{\partial r_{C(2,l),l}}{\partial v_{C(2,l)}} \end{bmatrix}$$

that is plugged in the global matrix as

$$\frac{\partial \mathcal{M}}{\partial \mathbf{v}_h} [C(h, l), C(g, l)] = \frac{\partial \mathbf{M}_l}{\partial \mathbf{v}_h} [h, g] \quad h, g = 1, 2.$$

Unlike the domain of air and panel, in the Jacobian matrix of the channel problem the only neglected derivatives are those of the terms calculated through empirical correlations, hence the approximation is more accurate.

All the single-phase physical properties of the refrigerant fluid are interpolated as a function of the temperature from saturation tables generated using the REFPROP software.

7.2 Boundary conditions

In this section we describe how to practically implement the boundary conditions for each problem.

Usually at the inflow boundary of each domain we have Dirichlet boundary conditions, there are two possible techniques of implementation [Qua08, p. 382]. We will compare them referring to a general algebraic problem $\mathcal{A}\mathbf{x} = \mathbf{B}$, where the l -th node is an inflow node and the value imposed at the boundary is x_0 .

The first more classical technique consists of deleting the l -th row of the matrix \mathcal{A} and moving the l -th column multiplied for x_0 to the right hand side.

The second approach is well known as *Irons trick* and consists in setting to zero the l -th row of \mathcal{A} , except the diagonal element set to one, then setting the l -th value of \mathbf{B} equal to the value of the solution at the boundary. This means that the Dirichlet boundary conditions are imposed as algebraic constraints $x[l] = x_0$ in the equations. The first technique described reduces the dimension of the matrix to solve, but at the same time changes significantly the pattern of the matrix. Instead the second method maintains the original size of \mathcal{A} , but affects the symmetry of the matrix which, in turn, can give rise to scaling problems.

We consider now the Neumann boundary conditions. The homogeneous one are settled automatically by the numerical method, while the non homogeneous one

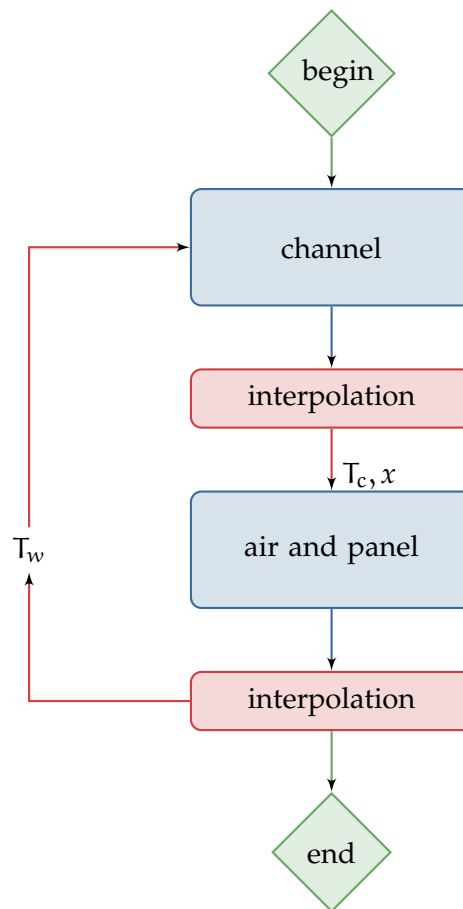


Figure 7.1: Iteration algorithm between domains.

are implemented adding a diagonal term to the matrix \mathcal{A} . For example, in the air problem at the outflow boundary we impose the condition of null outgoing conduction heat flux, from the implementation point of view this results in adding to the diagonal term of the m -th row, a contribution equal to the outgoing diffusion flow if m -th is an outgoing node.

7.3 Iteration between domains

The idea is to divide the whole domain of the condenser in two parts, the first part is the air and panel coupled domain and the second is the channel domain, and iterate between them until convergence.

The iterative algorithm is described in Figure 7.1: the two main steps, denoted by blue boxes, are the iterative solutions of the nonlinear algebraic systems, one

for each part, while the intermediate steps, denoted by red boxes, represent the interpolation process of the solution of a part in the domain corresponding to the other part. We notice how the two parts communicate through the values of two-phase fluid temperature T_c and vapor quality x and panel wall temperature T_w .

Part IV

Simulation Results

In this chapter we present the numerical results obtained using the numerical solver and algorithms described in Chapter 7. We will first discuss the simulation for the coupled air and panel domains and then we will focus on the channel domain for both cases of incompressible single-phase and compressible two-phase fluid.

8.1 Test for air and panel subsystems

We present and analyze the numerical results concerning the coupled system made by the air and panel domains coupled. The associated nonlinear algebraic system has been described in Section 7.1.2.

We consider a series of condenser panels spaced by the air thickness $S = 1\text{ cm}$, each panel has the structure depicted in Figure 8.1: the panel is a rectangular domain of size $0.49\text{ m} \times 0.252\text{ m}$, crossed by a circular channel of radius $r = 0.3\text{ cm}$.

First of all we consider the features of the discretization mesh used. In practice we have two separate meshes one for the channel domain, where each element is a vertical or horizontal trunk of channel, and a single cartesian rectangular mesh for the air and panel domains. To couple the two meshes we used the following criterion: if we superimpose the channel mesh to the air-panel mesh, each rectangular element that is partially covered by a channel mesh element is considered joining both meshes. In Figure 8.2 we can make a comparison between the two meshes used in the simulation, we have refined the channel mesh in such a way that the size of each trunk is less than or equal to $H = 1.7\text{ cm}$ and used a 100×100 air-panel mesh.

We consider the R134a refrigerant fluid flowing in the channel at constant tem-

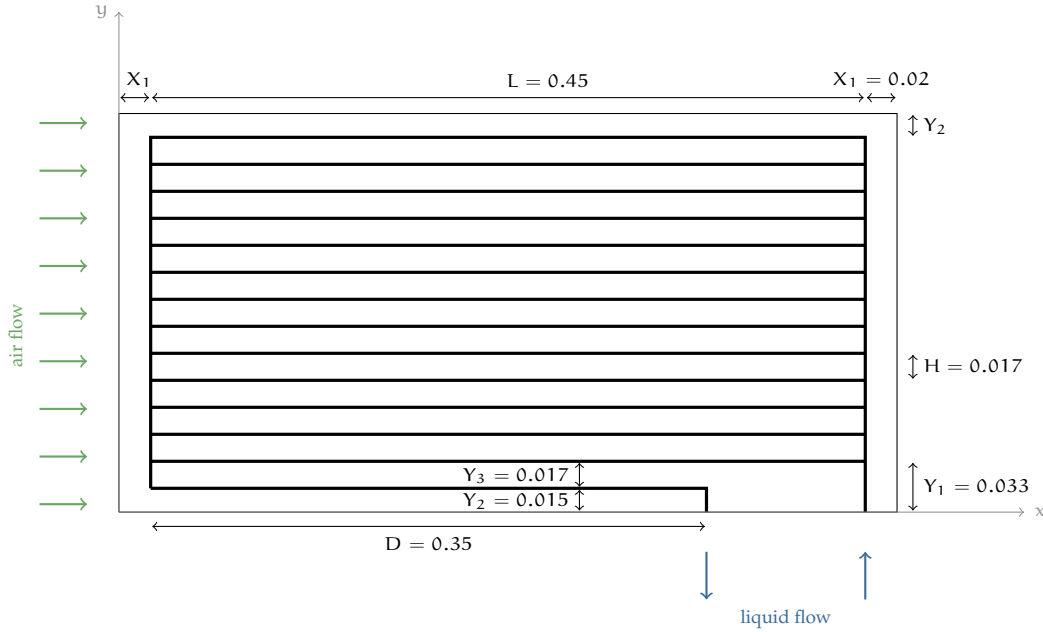


Figure 8.1: Air and panel coupled test case: geometry. The thick black line denotes the channel path in the rectangular panel domain, splitting in branches are considered. Lengths are measured in meters. The blue arrows denote the inlet and outlet boundary of the channel and the green arrows denote the air flow direction.

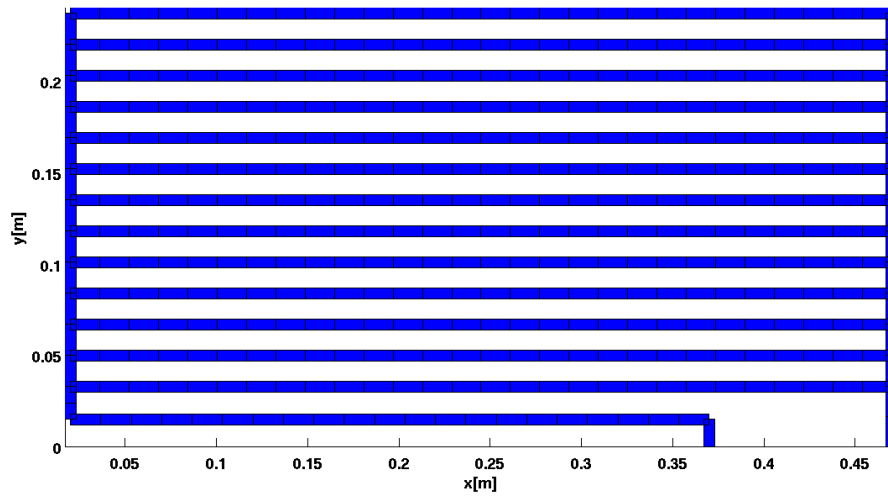
perature $T_c = 60^\circ\text{C}$, constant velocity of $v = 0.63\text{m/s}$ and constant vapor quality $x = 0.5$. The physical two-phase properties of this particular refrigerant fluid will be discussed in detail in Section 8.2.2.

Under these assumptions the heat transfer coefficient between the refrigerant fluid and the aluminum wall is constant $h_{wc} = 5.1727 \times 10^3\text{W/m}^2\text{K}$, this value being obtained using the Shah two-phase correlation (4.12) and the Dittus-Boelter correlation (2.7) for the single-phase heat transfer coefficients.

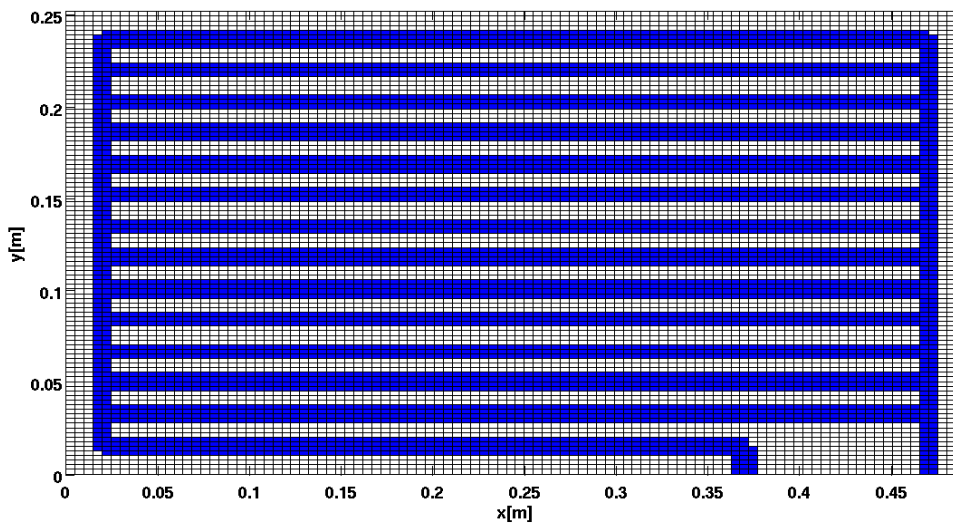
Concerning the air domain conditions, we fix a velocity of 10m/s from left to right, as depicted in Figure 8.1, and we impose the inlet boundary condition of $T_a = 45^\circ\text{C}$.

In Figure 8.3 we show the distribution of the air temperature T_a and of the wall temperature T_w and in Figure 8.4 the associated contour plot. The Newton method, used for solving the non linear algebraic system (7.4), in 27 iterations and 57.64s reaches convergence, setting the tolerance to 10^{-6} . The computed values of temperature have been interpolated through a nodally continuous function.

We can notice how the air temperature increase gradually flowing on the heated panel wall and how the distribution of the panel wall temperature is influenced by

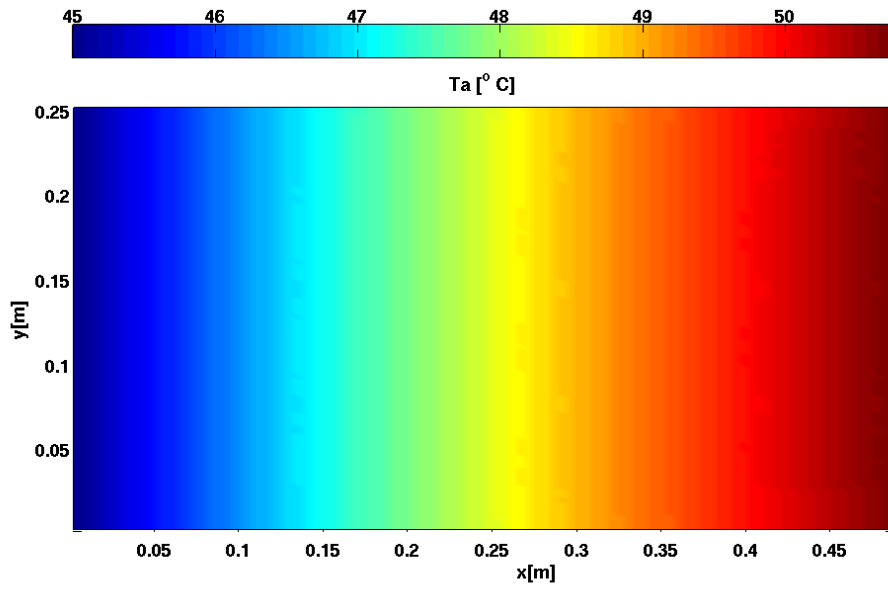


(a) channel mesh

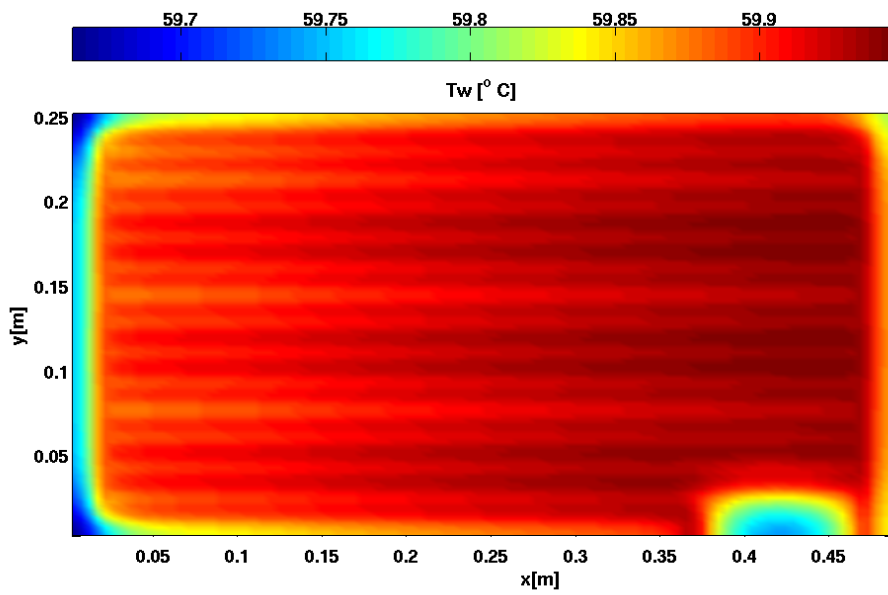


(b) air-panel mesh

Figure 8.2: Air and panel coupled test case: channel and air-panel meshes. Channel mesh has an element size less than or equal to $H = 1.7\text{cm}$ and the air-panel mesh has size 100×100 .

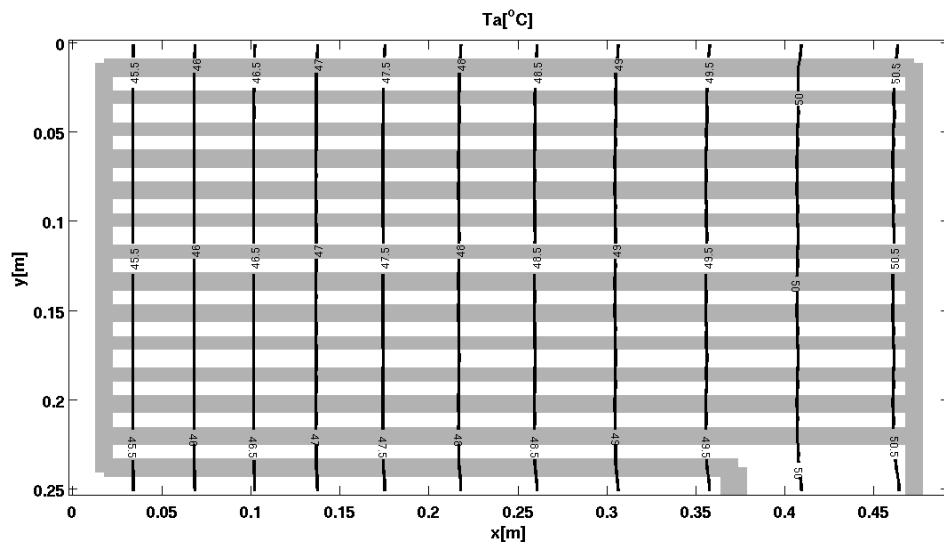


(a) air temperature

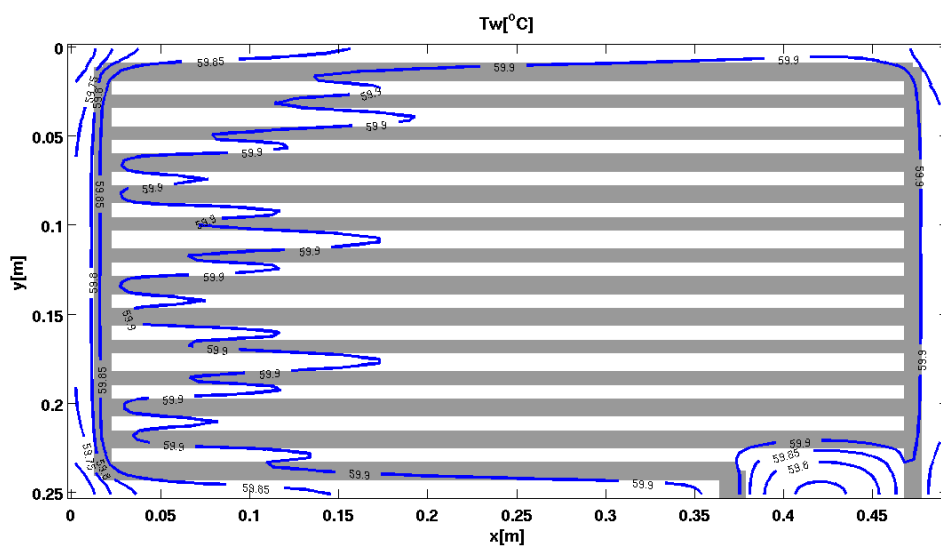


(b) panel temperature

Figure 8.3: Air and panel coupled test case: air temperature and panel wall temperature solution.



(a) air temperature



(b) panel temperature

Figure 8.4: Air and panel coupled test case: contour plot of air temperature and panel wall temperature solution.

the channel geometry, highlighted in the contour plot of Figure 8.4.

As mentioned in the introductory Chapter 1 and shown in Figure 1.4, the advantage of using two-phase cooling systems is provided by a higher value of the heat transfer coefficient. Indeed, the heat transfer coefficients $h_{wc} = 5.1727 \times 10^3 \text{W/m}^2\text{K}$ has two orders of magnitude more than h_{aw} , depicted in Figure 8.5(a). Consequently, the panel wall temperature is almost constant and very close to the two-phase flow temperature of 60°C . This confirms the interpretation of the condenser studied as a heat sink, where each panel is a fin with efficiency equal to one, having almost constant temperature in all the extended surface.

All the results shown till now are computed using the Dittus-Boelter (2.7) correlation, the entrance region correction of Bhatti and Shah (2.8) for h_{aw} and the approximation at the inlet cells described in Section 7.1.1. In Figure 8.5 we can notice how the fully developed Dittus-Boelter correlation under-predicts the heat transfer coefficient h_{aw} in the inlet transition flow region by a factor of 17%.

Concerning the air pressure drop, in Figure 8.6 we can analyze the exponential increase of the total pressure losses upon varying the air velocity from $1\text{m}/2$ to $20\text{m}/\text{s}$. By total air pressure drop we mean the difference between the air pressure at the inlet and outlet boundary for $x = 0\text{m}$ and $x = 0.49\text{m}$ respectively. The corresponding values of the friction factor f are calculated through the Bhatti and Shah correlation (2.10).

8.2 Test for channel subsystem

In this section we report the results of the numerical simulation concerning the cases of incompressible single-phase and of compressible two-phase fluid flow.

8.2.1 Single-phase incompressible fluid

We consider liquid-phase water flowing in the channel domain. The pattern of the channel is the same as in the previous test case, shown in Figure 8.1, where inlet and outlet boundaries are denoted by blue arrows, while the radius of channel circular cross section is $r = 0.6\text{cm}$. We will solve only the channel domain problem, imposing constant panel wall temperature $T_w = 45^\circ\text{C}$ and using the same mesh as in Figure 8.2(a).

Concerning the inlet boundary condition, we impose fluid temperature of 60°C and fluid velocity of $1\text{m}/\text{s}$, hence the corresponding mass flow is $G = 0.1112\text{kg}/\text{s}$. Moreover, we assume constant water physical properties equal to the values listed in Table 8.1, corresponding to the water at the inlet temperature of 60°C .

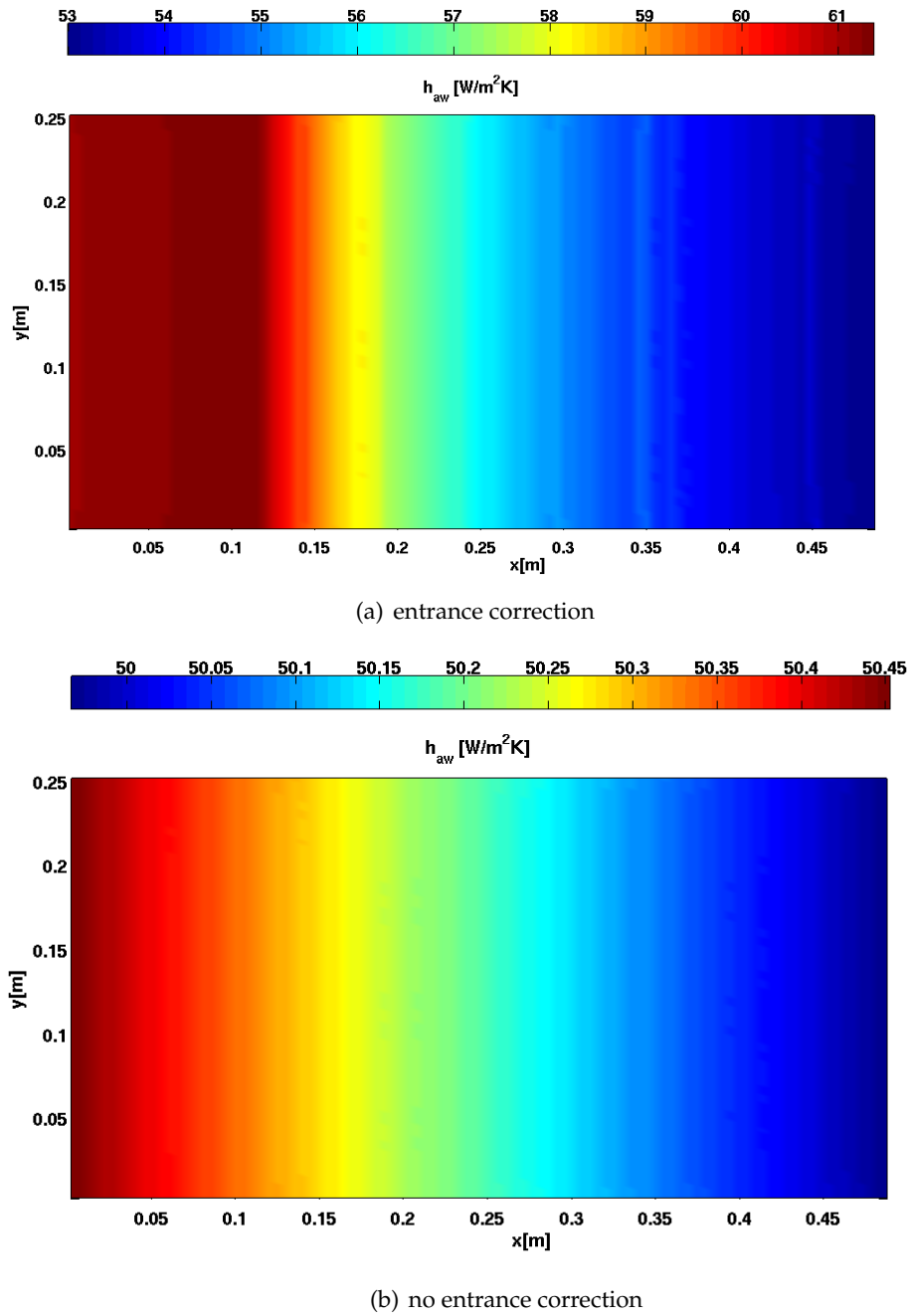


Figure 8.5: Air and panel coupled test case: heat transfer coefficient h_{aw} using or not using the Bhatti and Shah (2.8) entrance correction.

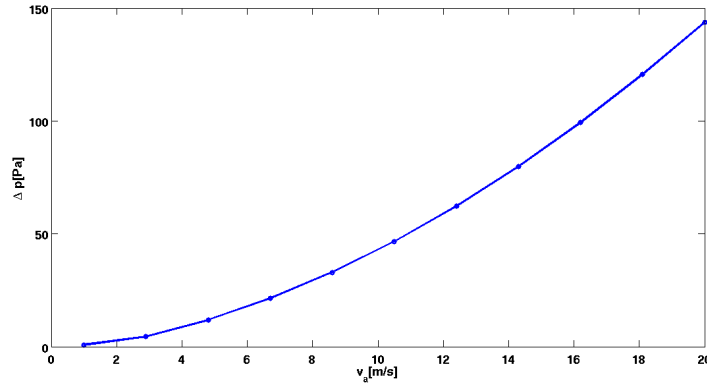


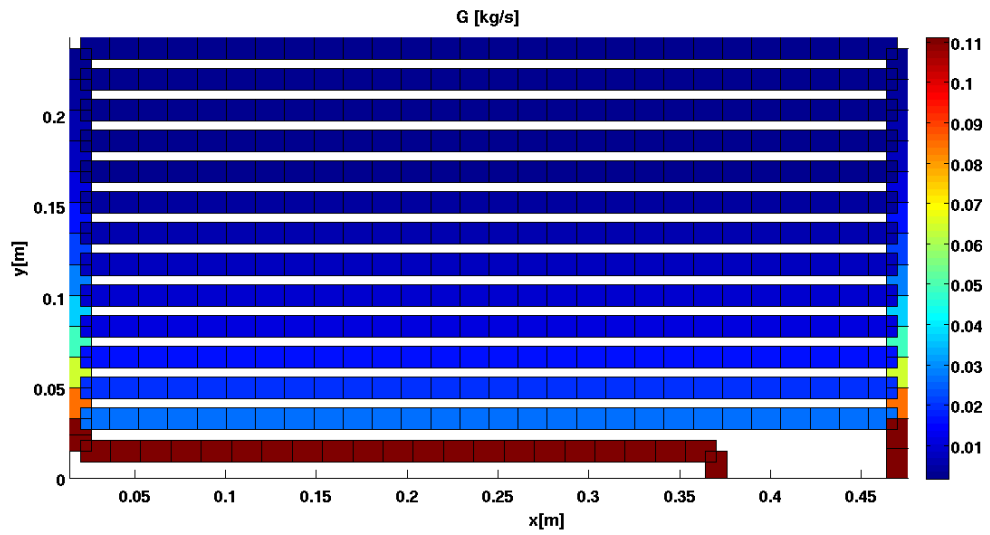
Figure 8.6: Air and panel coupled test case: total air pressure drop varying the inlet air velocity v_a .

$\rho = 983.2 \text{ kg/m}^3$	density
$\mu = 0.4668 \times 10^{-3} \text{ Pa}\cdot\text{s}$	dynamic viscosity
$c_v = 3981.5 \text{ J/kgK}$	specific heat capacity at constant volume
$k = 0.6 \text{ W/mK}$	thermal conductivity

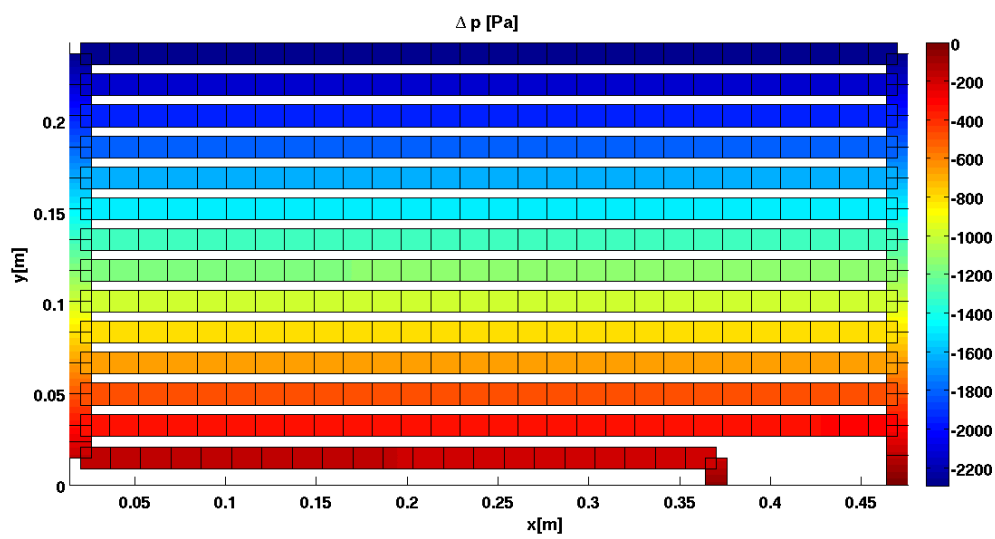
Table 8.1: Water physical properties at the temperature of 60°C .

In Figure 8.7 we show the solution obtained for the mass and momentum balance equation, where we denote by G the mass flow \dot{m} . The mass balance equation is satisfied because the mass flux at the outlet boundary is equal to the value imposed at the inlet. Instead, in Figure 8.7(b) the pressure drop calculated in node is the difference between the pressure in the node and the pressure at the inlet boundary of the channel, hence the value of Δp at the channel outlet boundary is the whole channel pressure drop.

Also in the case of single-phase fluid we can interpret the total pressure drop as the sum of three contributions: static, momentum and frictional pressure drops, as described in Section 4.3.2 for the two-phase fluid. These contributions can be computed a posteriori, in the test case considered the results are depicted in Figure 8.8. We notice that the whole static pressure drop is null, since the inlet and outlet boundary are located at the same height. Instead, the order of magnitude of the momentum pressure drop verifies the assumption of the model used, in fact this effect has been neglected in equation (4.3). The frictional pressure drop contribution is the only relevant and is equal to the term $-R\dot{m}$ of equation (4.3), where R is the hydraulic resistance of the whole channel.

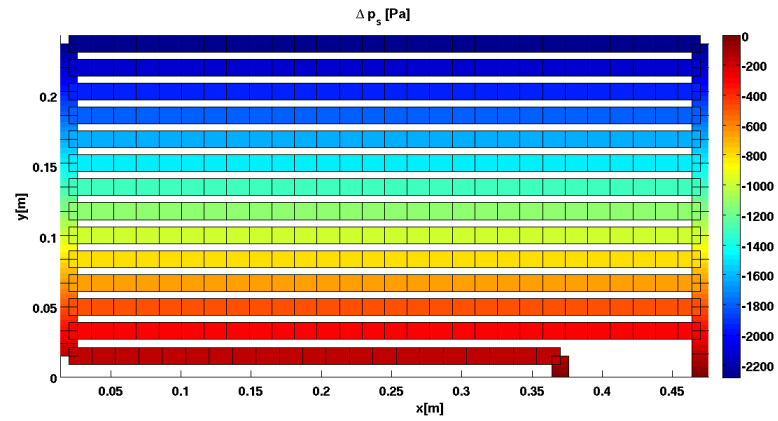


(a) mass flow

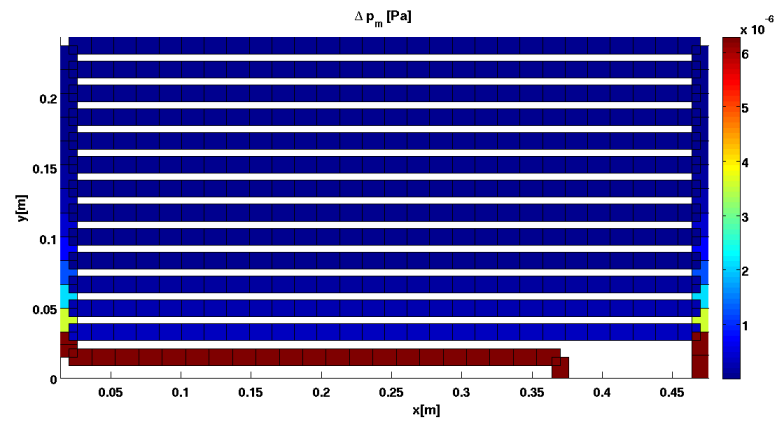


(b) total pressure drop

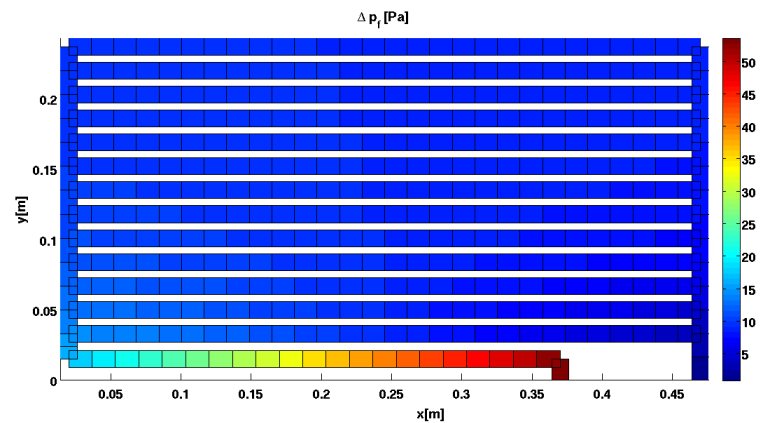
Figure 8.7: Incompressible single-phase test case: mass flow G and total pressure drop Δp . In each node the pressure drop is equal to the difference between the pressure of the node and the inlet water pressure.



(a) static pressure drop



(b) momentum pressure drop



(c) frictional pressure drop

Figure 8.8: Incompressible single-phase test case: three contributions to the total pressure drop. In each node the pressure drop is equal to the difference between the pressure of the node the inlet water pressure.

To validate the robustness of the results shown in Figure 8.8(c) we can calculate the hydraulic resistance of the channel using the analogy with an electric circuit: each trunk of channel is equivalent to an electric resistance and at the inlet and outlet boundary are connected two suitable current or voltage generators.

The expression of the resistance corresponding to the whole channel is

$$R_{\text{tot}} = R \left[Y1 + \frac{1}{R_L + \frac{1}{L}} + Y3 + Y2 \right],$$

where the value of $Y1$, $Y2$, $Y3$ and L are the same as in Figure 8.1 and $R_L = 0.1422\text{m}^{-1}$ is the continued fraction $[2H; 1/L]$, i.e. expressed recursively as

$$\begin{cases} R_L^1 &= 2H + L, \\ R_L^{i+1} &= 2H + \frac{1}{\frac{1}{L} + \frac{1}{R_L^i}} \quad \forall i \geq 1. \end{cases}$$

R_L is the contribution to the total resistance due to the part of the channel where are all the splitting in branches, i.e. $y \geq Y1$. In conclusion, being $R = 932.876\text{m}^{-2}\text{s}^{-1}$, the theoretical value of friction pressure losses at the outlet boundary is

$$\Delta p_f = -R_{\text{tot}} G_{\text{out}} = -432.878\text{m}^{-1}\text{s}^{-1} \times 0.1112\text{kgs}^{-1} = -54.3619\text{Pa},$$

almost equal to the computed value of -54.3622Pa .

In Figure 8.9 we show the distribution of water temperature in two cases:

- h_{wc} constant: the fixed value is calculated through the Dittus-Boelter correlation at the inlet fluid temperature of 60°C ,
- h_{wc} varies linearly: h_{wc} depends on the water temperature through the Dittus-Boelter, this trend is approximated by a linear fitting.

In the second case the water flowing in the channel cools more slowly because h_{wc} decrease linearly reducing the water temperature. Consequently, we decided to investigate the variation of the outlet water temperature as a function of the constant T_w in both cases of h_{wc} constant or linearly varying. Figure 8.10 shows the importance of the dependence of the heat transfer coefficient by the water temperature, otherwise there is a significant under-prediction of the outlet water temperature, i.e. a over-prediction of the cooler efficiency.

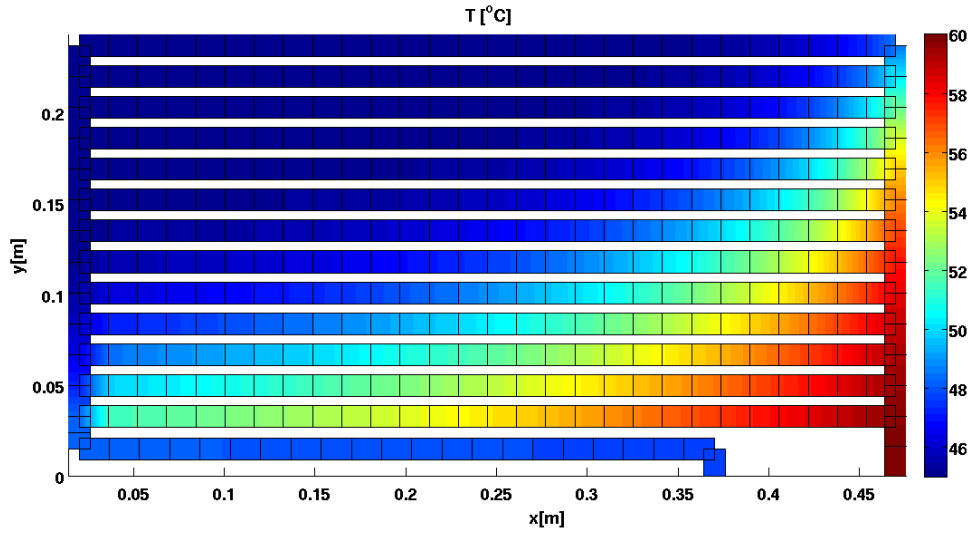
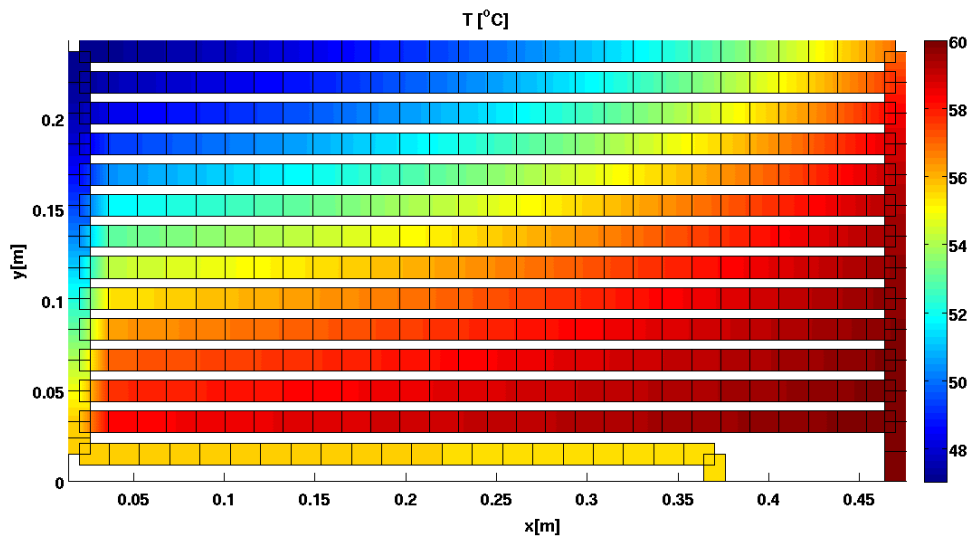
(a) h_{wc} constant(b) h_{wc} Dittus-Boelter

Figure 8.9: Incompressible single-phase test case: temperature distribution with h_{wc} constant or that varies linearly as function of the water temperature, through the Dittus-Boelter (2.7) correlation.

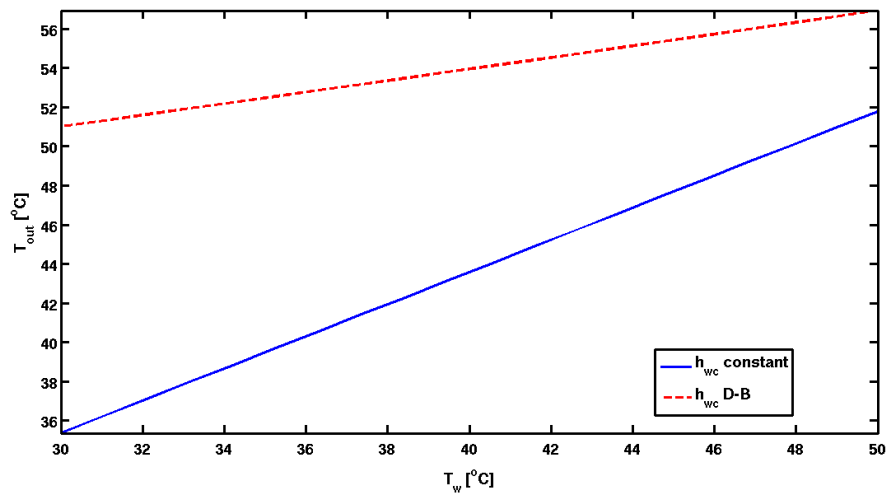


Figure 8.10: Incompressible single-phase test case: variation of the outlet water temperature T_{out} as a function of the fixed wall temperature T_w , with h_{wc} constant or varying according to Dittus-Boelter (2.7) correlation.

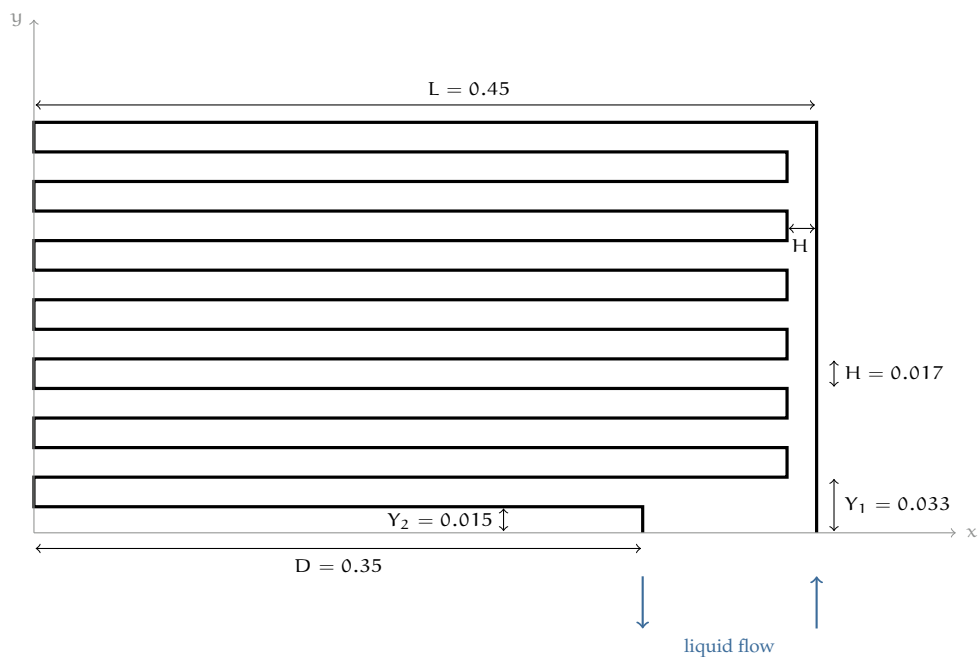
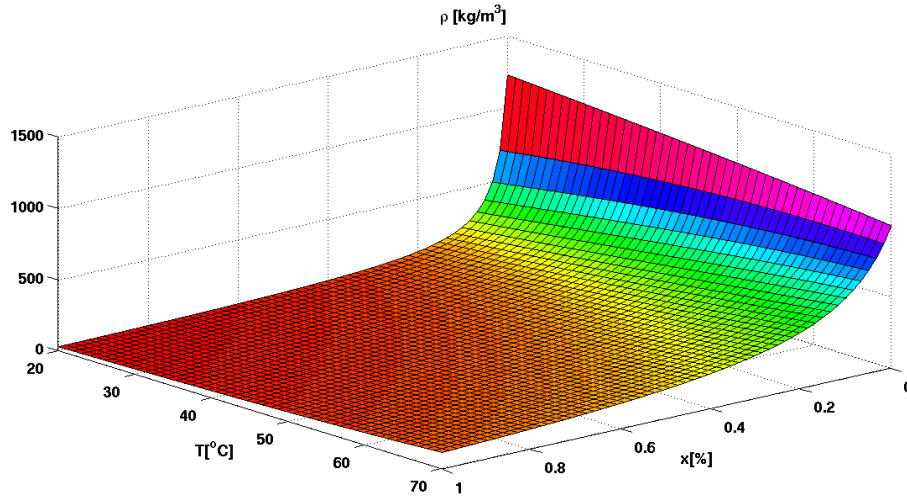
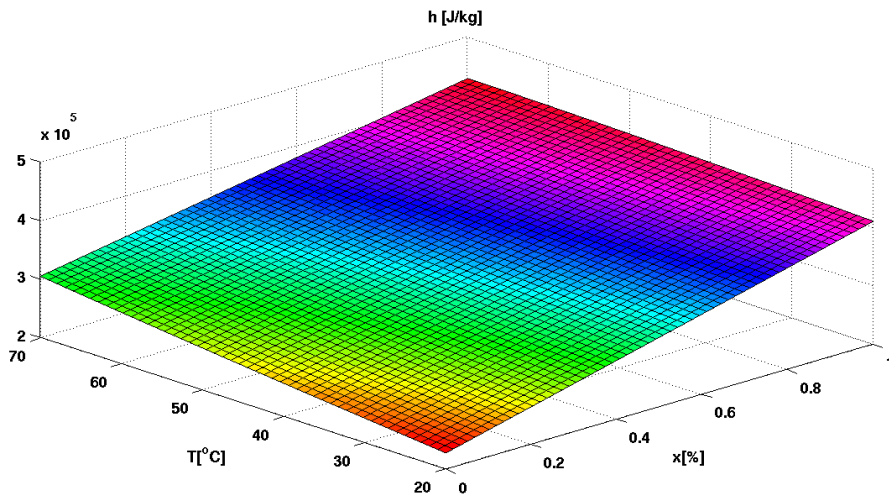


Figure 8.11: Compressible two-phase test case: geometry. The thick black line denotes the channel path no splitting in branches are considered. Lengths are measured in meters. The blue arrows denote the inlet and outlet boundary of the channel.



(a) two-phase density



(b) two-phase enthalpy

Figure 8.12: Compressible two-phase test case: R134a two-phase properties.

8.2.2 Two-phase compressible fluid

We consider now the R134a refrigerant fluid flowing in the circular channel of geometry described in Figure 8.11: there are no splittings in branches and the channel cross sectional radius is $r = 0.6\text{cm}$. First of all, in Figure 8.12, we analyze the dependence of the R134a two-phase density and enthalpy on the vapor quality x and on the refrigerant temperature, accordingly to the first two the constitutive

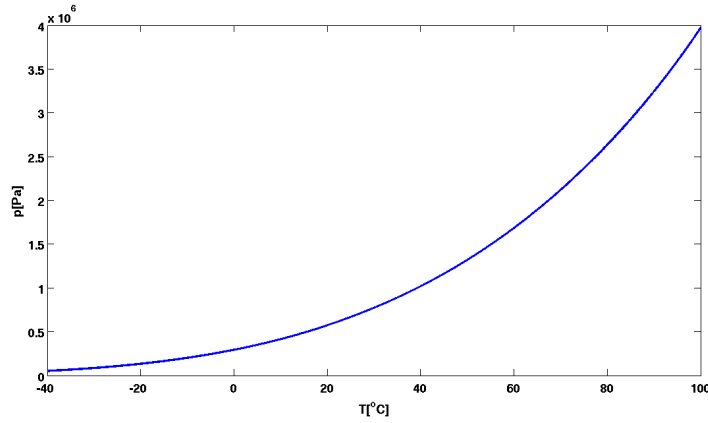


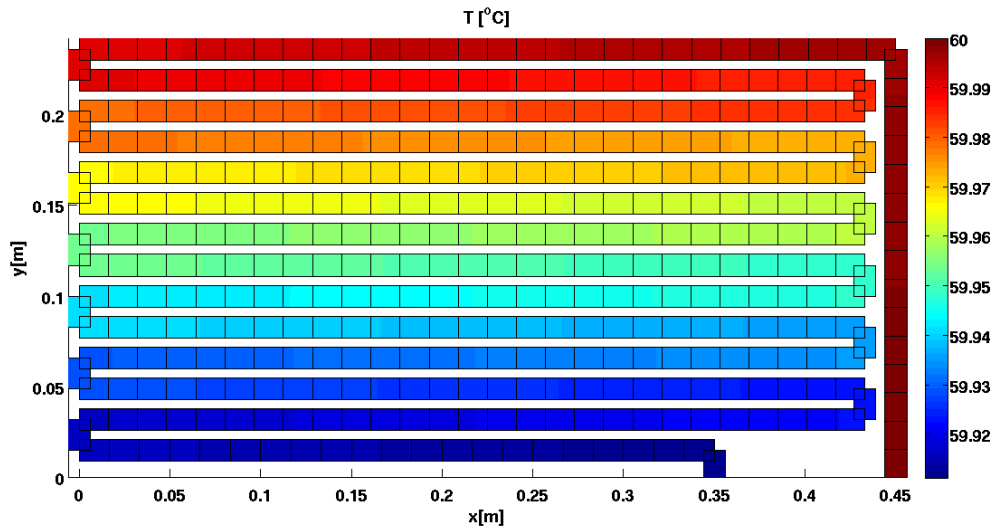
Figure 8.13: Compressible two-phase test case: R134a saturation pressure-temperature curve.

relations of (4.11). As expected, fixing the water temperature these two-phase properties grow increasing with the vapor quality x : the density exhibits an exponential growth and the enthalpy a linear one. The trend of the third constitutive equation of (4.11) for the R134a fluid is plotted in Figure 8.13: on the saturation curve the pressure has an exponential trend when temperature is varying.

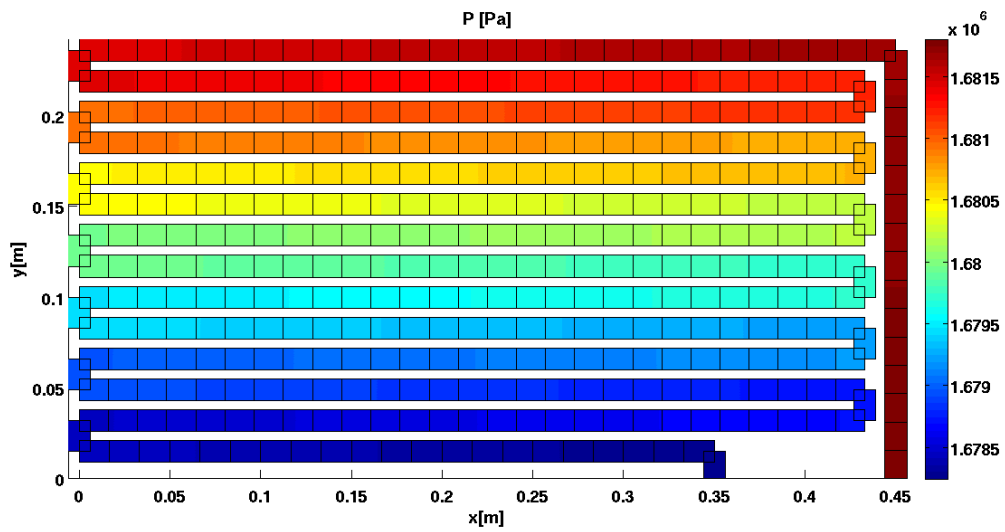
In the next simulation results we have fixed the wall temperature equal to $T_w = 50^\circ\text{C}$ and we have solved only the channel domain problem using a mesh such that the size of each element is less than or equal to $H = 1.7\text{cm}$. We impose an inlet refrigerant temperature of 60°C , hence the corresponding inlet pressure is $1.6818 \times 10^6\text{Pa}$ according to the saturation curve in Figure 8.13. We impose also the inlet boundary the fluid velocity $v = 5\text{m/s}$ and the inlet vapor quality $x = 1$, consequently the inlet mass flux ρv and the inlet two-phase enthalpy are uniquely determined.

Under this working assumptions, the numerical solutions obtained are depicted in Figures 8.14 and 8.15. From the computational point of view, the Newton method reaches convergence in 19 iterations and 83.277s, setting the tolerance to 10^{-6} . All the unknown variables show a decreasing trend, effect of the cooling phenomenon. In fact, at fixed temperature the liquid-phase properties are lower than the corresponding vapor-phase properties, as illustrated in Figure 8.12.

In Figure 8.14(a) we can notice the small gap between the inlet and the outlet refrigerant temperature, verifying one advantage of the two-phase cooling system. Indeed, the heat handed over by the refrigerant fluid produces a change of phase, hence a relevant variation of vapor quality x and only an irrelevant decrease of the fluid temperature.



(a) temperature



(b) pressure

Figure 8.14: Compressible two-phase test case: R134a temperature and pressure.

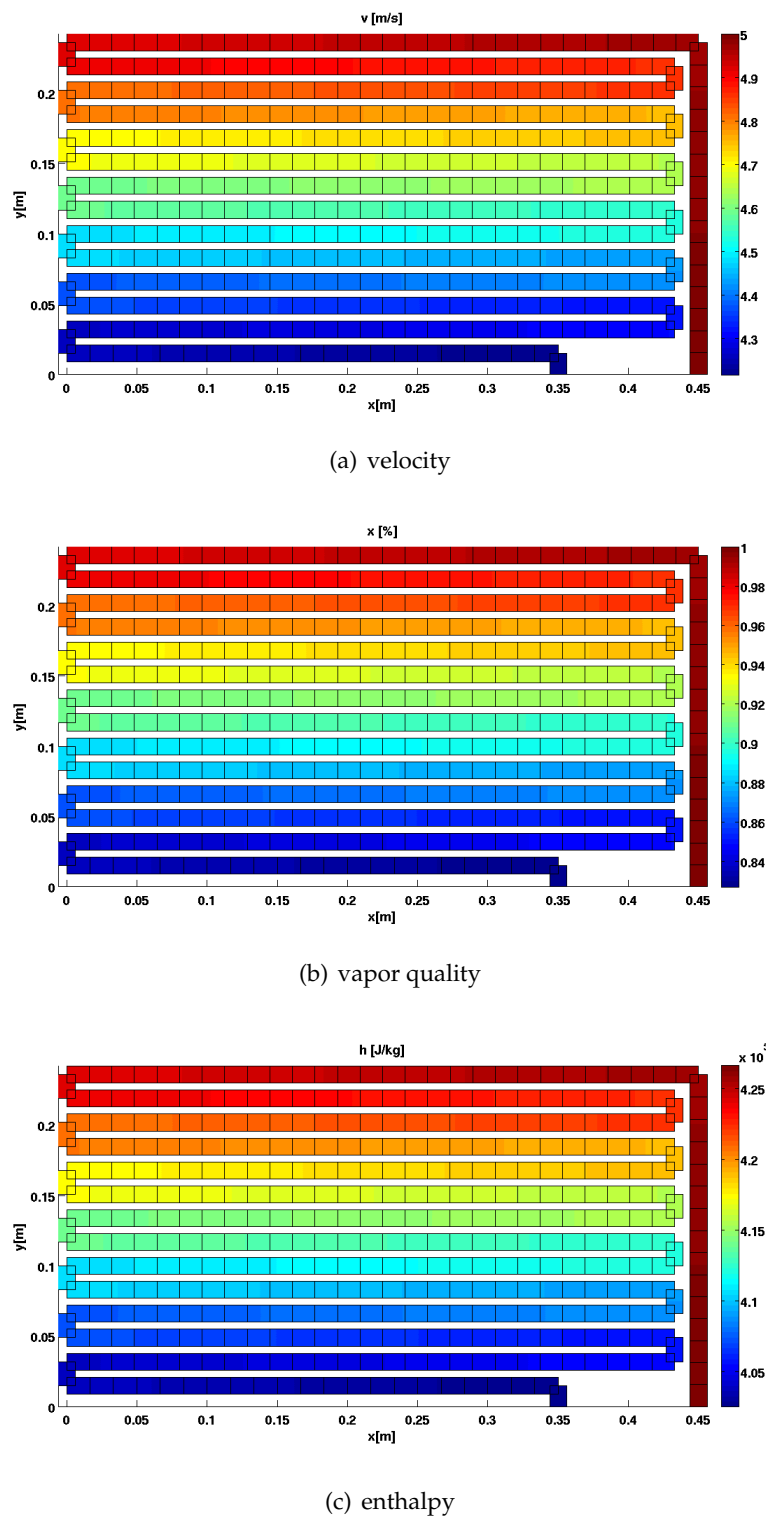


Figure 8.15: Compressible two-phase test case: R134a velocity, vapor quality and two-phase enthalpy.

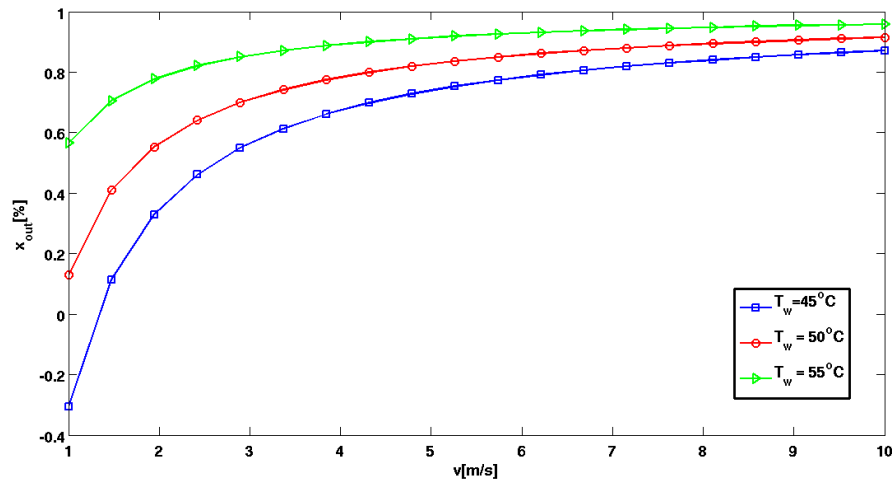


Figure 8.16: Compressible two-phase test case: outlet vapor quality as a function of the inlet fluid velocity for three different cases of constant wall temperature.

To investigate which are the optimal conditions of this condenser, in Figure 8.16 at three different panel wall temperatures we show the variation of the outlet vapor quality as a function of the inlet flow velocity. We can conclude that for the lowest values of velocity we obtain the lowest value of outlet x . In the case of $T_w = 45^\circ\text{C}$ the vapor quality is negative, this phenomenon is called *subcooling*, which means that the two-phase flow once achieved totally the liquid face continues to cool itself being in contact with the aluminum wall.

Part V

Conclusions and Perspectives

Conclusions and future work

In the present Master thesis we have addressed the mathematical modeling and numerical simulation of a specific air-cooled condenser, part of the ABB industrial research on the optimal design for a two-phase thermosyphon cooling system.

The main targets and obtained results can be summarized in three parts:

Mathematical models: a reduced-order modeling approach has been extensively used to derive simplified mathematical descriptions of the various subsystems involved in the device setting and configurations. Such reduced-order models represent a good compromise between physical accuracy and computational effort, and can be regarded as an original and significant contribution of the present thesis.

Numerical methods: conservative discretization schemes have been adopted in order to maintain the conservative form of the equations on the discrete level. Furthermore, the corresponding compact computational stencil ensures good properties of the algebraic systems. Suitable stabilization techniques have been introduced in order to avoid the onset of spurious oscillations in dominating convection regimes, even in the limit of vanishing viscosity. An approximate Jacobian matrix has been introduced in the iterative Newton method; extensive computational experiments show that, at the price of slightly increasing the number of iterations required to reach convergence, there is a substantial reduction of the elapsed CPU time, compared to a full exact Newton solution.

Numerical results: a simulation tool has been implemented in view of a day-by-day design of advanced cooling system in power electronics. The ultimate requirement for ABB designers, which has constantly driven the research ac-

tivity of this thesis, has been the computational efficiency and robustness with respect to physical model parameters and, last but not least, a high user friendliness of the computer routines. All of these constraints have been successfully satisfied and implemented in the final version of the software developed for numerical simulation. The discussed results are aimed to validate the performance of the proposed computational model in the study of the main device configurations; all simulations have been performed using always realistic values of geometrical data and parameters and all the corresponding outcome of the computations agree with engineering based physical predictions.

Future research is, of course, needed in order to provide a better description of the very complex multiscale/multiphysics problem addressed in the present thesis. Among possible developments, we mention:

Natural convection: in the current model and in the numerical simulation we have always assumed the air convection field to be fixed, i.e., that device operate in forced convection regime. In practice it is often useful to consider the case of natural convection, i.e., the convection be self consistently dependent on the panel wall temperature, to incorporate this phenomenon in our model requires extending the simple iteration algorithm of Section 7.3 to cope with the stronger coupling among the air, panel and channel subsystems.

Different two-phase flow regimes: as mentioned in Section 1.2 the properties of the two-phase flow strongly depend on the particular pattern of the flow, see Figure 1.7. To take into account the effect of the flow regime change on the vapor/liquid mixture properties requires relaxing the homogeneous flow assumption of Section 4.2.1, which also requires adding an additional unknown to the system namely void fraction.

Singular pressure losses: to more correctly model the junctions and bends in the channel requires including specific empirical correlations for the frictional pressure drops depending on the particular geometry of non straight channel segments. A comprehensive catalog of such correlations can for example be found in [IF86], alternatively full three-dimensional simulations could be used to obtain correlations for geometries that have not yet been considered.

Bibliography

- [BFM93] F. Brezzi, M. Fortin, and D. Marini, *Mixed finite element methods with continuous stresses*, *Mathematical Models and Methods in applied sciences* **3** (1993), no. 2, 275–28.
- [BH82] A.N. Brooks and T.J.R. Hughes, *Streamline upwind/Petrov-Galerkin formulations for convection dominated flows with particular emphasis on the incompressible Navier-Stokes equations*, *Computer methods in applied mechanics and engineering* **32** (1982), no. 1-3, 199–259.
- [CCDC⁺03] A. Cavallini, G. Censi, D. Del Col, L. Doretti, GA Longo, L. Rossetto, and C. Zilio, *Condensation inside and outside smooth and enhanced tubes—a review of recent research*, *International Journal of Refrigeration* **26** (2003), no. 4, 373–392.
- [CT96] J.G. Collier and J.R. Thome, *Convective boiling and condensation*, Oxford University Press, USA, 1996.
- [GV03] O. Garcia-Valladares, *Review of in-tube condensation heat transfer correlations for smooth and microfin tubes*, *Heat Transfer Engineering* **24** (2003), no. 4, 6–24.
- [HRB75] Chung-Wen Ho, A. Ruehli, and P. Brennan, *The modified nodal approach to network analysis*, *Circuits and Systems, IEEE Transactions on* **22** (Jun 1975), no. 6, 504–509.
- [IDW02] F.P. Incropera and D.P. De Witt, *Fundamentals of heat and mass transfer*, John Wiley and Sons Inc., New York, NY, 2002.

- [IF86] IE Idelchik and E. Fried, *Handbook of hydraulic resistance*, Hemisphere Publishing, New York, NY, 1986.
- [KSA87] S. Kakaç, R.K. Shah, and W. Aung, *Handbook of single-phase convective heat transfer*, Wiley New York et al., 1987.
- [LL87] LD Landau and EM Lifshitz, *Course of Theoretical Physics. Volume 6: Fluid Mechanics*, Butterworth-Heinemann, 1987.
- [MSH86] H. Müller-Steinhagen and K. Heck, *A simple friction pressure drop correlation for two-phase flow in pipes*, *Chemical Engineering and Processing: Process Intensification* **20** (1986), no. 6, 297–308.
- [QSS08] A. Quarteroni, R. Sacco, and F. Saleri, *Matematica numerica*, Springer, 2008.
- [QT05] J.M. Quibén and JR Thome, *Experimental and analytical study of two-phase pressure drops during evaporation in horizontal tubes*, Ph.D. thesis, École polytechnique fédérale de Lausanne, 2005.
- [Qua08] A. Quarteroni, *Modellistica numerica per problemi differenziali*, Springer, 2008.
- [QV08] A.M. Quarteroni and A. Valli, *Numerical approximation of partial differential equations*, Springer Verlag, 2008.
- [RA70] S.Z. Rouhani and E. Axelsson, *Calculation of void volume fraction in the subcooled and quality boiling regions*, *International Journal of Heat and Mass Transfer* **13** (1970), no. 2, 383–393.
- [Sal04] S. Salsa, *Equazioni a derivate parziali. Metodi, modelli e applicazioni*, Springer, 2004.
- [Sha79] MM Shah, *A general correlation for heat transfer during film condensation inside pipes*, *International Journal of Heat and Mass Transfer* **22** (1979), no. 4, 547–556.
- [SS97] R. Sacco and F. Saleri, *Stabilized mixed finite volume methods for convection-diffusion problems*, *East-West Journal of Numerical Mathematics* **5** (1997), no. 4, 291–311.
- [Tho06] J.R. Thome, *Engineering Data Book III*, Wolverine Tube, Inc, 2006.

-
- [Wha96] P.Bb Whalley, *Two-phase flow and heat transfer*, Oxford University Press Oxford, 1996.
- [XZ99] J. Xu and L. Zikatanov, *A monotone finite element scheme for convection-diffusion equations*, *Mathematics of Computation* **68** (1999), no. 228, 1429–1446.